Machine learning compliance calibration for local fatigue energy release rate calculations in multi-directional laminates with fiber bridging

Amkies, Roy; Pascoe, John Alan; van der Panne, Mike; Mega, Mor

DOI
10.1016/j.engfracmech.2025.111289

Publication date
2025

Document Version
Final published version

Published in
Engineering Fracture Mechanics

Citation (APA)
Amkies, R., Pascoe, J. A., van der Panne, M., & Mega, M. (2025). Machine learning compliance calibration for local fatigue energy release rate calculations in multi-directional laminates with fiber bridging. *Engineering Fracture Mechanics*, *325*, Article 111289. https://doi.org/10.1016/j.engfracmech.2025.111289

Engineering Fracture Mechanics 325 (2025) 111289

Contents lists available at ScienceDirect

Engineering Fracture Mechanics

journal homepage: www.elsevier.com/locate/engfracmech

Machine learning compliance calibration for local fatigue energy release rate calculations in multi-directional laminates with fiber bridging

Roy Amkies [a,*], John-Alan Pascoe [b], Mike van der Panne [b], Mor Mega [a]

[a] Department of Mechanical Engineering & Mechatronics, Ariel University, Ariel, 407000, Israel
[b] Department of Aerospace Structures and Materials, Faculty of Aerospace Engineering, Delft University of Technology, Kluyverweg 1, 2629 HS Delft, The Netherlands

ARTICLE INFO

Keywords:
Delamination growth
Fatigue
Fiber bridging
Finite elements
Multi-directional laminate

ABSTRACT

This study presents a numerical analysis framework of multidirectional (MD) composite laminate under mode I fatigue loading, with calibration to account for fiber bridging. Both local and global methods for calculating the energy release rate are compared. Seven unidirectional (UD) and MD layups were tested, revealing differences in fatigue resistance based on fiber orientation and initial delamination length. Fiber bridging, where fibers stretch across separating plies, was found to enhance toughness. The results show that fiber bridging intensity varies with fiber orientation, with minimal stiffening for the 0°//0° interface and significant stiffening for 90°//90°, 0°//45°, and 0°//90° interfaces.

1. Introduction

Composite materials are often desired for their better mechanical properties and performance. In the aviation industry, where weight and manufacturing costs play a major role in design considerations, research of laminate composites is a great challenge that requires massive testing and complex analyses to evaluate the structural integrity of every new layup or design. Laminated composites are assembled from stacked unidirectional (UD) or woven plies. Often, the plies within a laminate layup differ in orientation in order to reach specific engineering properties. Such laminates are referred to as Multi-Directional (MD) laminates.

One of the leading mechanisms of failure in composite laminates is delamination. Delaminations are caused by high interlaminar stresses in conjunction with the typically low through-thickness strength. The phenomenon arises because fibers lying in the plane of a laminate do not reinforce the thickness. So, the composite relies on the relatively weak matrix to carry loads in that direction [2]. Delaminations may be initiated due to stress singularities caused by material or structural discontinuities, impact, or external loads. Although composite materials are relatively resistant to fatigue [3], undetected damage may result in catastrophic failure sooner than predicted.

It is common that for UD and MD composite laminates, the resistance energy release rate values in mode I, mode II, or mixed mode I/II deformations, $\mathcal{G}_{IR}$, $\mathcal{G}_{IIR}$ and $\mathcal{G}_{I/IIR}$, respectively, measured during delamination propagation, will be higher than the fracture toughness or critical energy release rate (ERR) values, measured at initiation [4–7]. This phenomenon may be modeled with a resistance curve or an *R*-curve. The *R*-curve represents the energy released as the delamination propagates $\mathcal{G}_R$. It begins at the critical delamination initiation value $\mathcal{G}_c$ and increases until reaching a steady state value $\mathcal{G}_{ss}$. Investigations of delamination propagation under quasi-static loading [7–15], indicate that the *R*-curve behavior depends on the fiber orientation which influences

* Corresponding author.
E-mail address: Royam@ariel.ac.il (R. Amkies).

https://doi.org/10.1016/j.engfracmech.2025.111289
Received 26 December 2024; Received in revised form 23 April 2025; Accepted 27 May 2025
Available online 11 June 2025

Nomenclature

a	The current delamination length measured from the load-line
a_f	The final delamination length in a fatigue test obtained from measurements
$a_{iFE} (i = 1, 2, 3, 4)$	Delamination length values assigned in the DCB FE model
a_0	The initial delamination length of each specimen, measured from the load-line
$\hat{a}$	Delamination length a normalized by the initial delamination length a_0
b	Width of a DCB specimen illustrated in Fig. 1
$2h$	Total DCB specimen height illustrated in Fig. 1
k	Percent change of a material property within a predefined range
l	Total length of a DCB specimen illustrated in Fig. 1
$\hat{l}$	Length parameter in the RBF kernel function
m	Slope of the line relating the compliance C, measured from the test, and the cubed delamination length a^3 in Eq. (9) used to determine a continuous function of a
n	A fitting parameter in Paris relation Eq. (1)
x_1	The coordinate oriented towards the delamination propagation direction
x_2	The coordinate along the specimen height or thickness
x_3	The coordinate along the delamination front through the specimen width
x_i, x_j	Close input points in the RBF kernel function
A_1	The slope of the delamination length normalized by the thickness $a/2h$ with respect to the third root of the compliance $C^{1/3}$ in Eq. (13) from the ASTM D5528 standard [1].
$B_i (i = 1, 2)$	Fitting parameters in Eq. (11) relating the delamination length a and the cycle number N
B_t	The ratio between bending stiffness components in the $\boldsymbol{D}$ matrix
C	Specimen compliance
C_0^{FE}	The compliance obtained from the FE model with the original material properties from the literature
C_k^{FE}	The compliance obtained from the FE model with a $k\%$ increase in a single material property
C_0	Intercept of the line relating the compliance C_{test}, measured from the test, and the cubed delamination length a^3 in Eq. (9) used to determine a continuous function of a
$C_i (i = 1, 2)$	Fitting parameters in Eq. (11) relating the delamination length a and the cycle number N
C_{FE}	Compliance obtained from the FE DCB model
C_{test}	Compliance obtained from a DCB test using Eq. (8)
D_c	The inverse ratio of the plane stress to plane strain rigidities
$D_i (i = 1, 2, 3)$	Fitting parameters in Eq. (16) relating the width averaged mode I ERR from FEA $\overline{\mathcal{G}}_{IFE}$ with the normalized delamination length $\hat{a}$
$D_{ij} (i, j = 1, 2, 6)$	Components of the $\boldsymbol{D}$ matrix
E_A	Young's modulus in the axial fiber direction
E_T	Young's modulus in the transverse fiber direction
G_A	Shear modulus in the axial fiber direction
G_T	Shear modulus in the transverse fiber direction
K	The RBF kernel function used in the MLR model
N	Fatigue test cycle number
P_{max}	Maximal load in a cycle
P_{min}	Minimal load in a cycle
R_d	Displacement ratio calculated from Eq. (6)
R_P	Load ratio calculated from Eq. (7)
$\overline{\mathcal{G}}_{IFE}$	The integrated average mode I ERR with respect to the specimen width x_3 obtained from FEA.
$\mathcal{G}$	Energy release rate
$\mathcal{G}_c$	Critical initiation energy release rate
$\mathcal{G}_m (m = \mathrm{I}, \mathrm{II}, \mathrm{III})$	Energy release rate related to the pure deformation mode m
$\mathcal{G}_R$	Fracture resistance energy release rate
$\mathcal{G}_c$	Critical initiation energy release rate or fracture toughness
$\mathcal{G}_{mc}$ (m = I,II,III)	Mode I, II or III critical initiation energy release rate
$\mathcal{G}_{mR}$ (m = I,II,III)	Mode I, II or III fracture resistance energy release rate

$\mathcal{G}_R$	Fracture resistance energy release rate
$\mathcal{G}_{ss}$	Steady state energy release rate
$\mathcal{G}_{tip}$	Energy release rate at the delamination tip excluding fiber-bridging tractions
$\mathcal{G}_{IC(a-a_0)}$	Energy release rate calculated at a given delamination extension length $a - a_0$ where a is the current delamination length and a_0 is the initial delamination length
$\mathcal{G}_{IC0}$	Mode I fracture toughness at no delamination growth
$\mathcal{G}_{Imax}$	Maximal mode I energy release rate in a cycle
$\mathcal{G}_{max}$	Maximal energy release rate in a cycle
P	Measured load
$P^{(FE)}$	The load employed in the FEAs for each specimen
Δa	Delamination length increment
ΔC	Percent difference between the measured compliance from testing C^{Test} and the compliance obtained from FEA C^{FE}, shown in Eq. (19)
ΔC^{FE}	Percent difference between the compliance from FEA with a $k\%$ increase in a material property C_k^{FE} and the compliance from FEA with the original material properties C_0^{FE}, shown in Eq. (18)
ΔC_{min}^{GPR}	The minimal percent difference between the measured compliance from testing C^{Test} and the compliance obtained from FEA C^{FE} predicted by the GPR model
ΔC_{min}	The minimal percent difference between the measured compliance from testing C^{Test} and the compliance obtained from FEA C^{FE} for a given set of material properties
ΔK	Amplitude of the stress intensity factors
δ	Mode I opening displacement
δ_{max}	Maximal displacement
δ_{min}	Minimal displacement
ν_A	Poisson's ratio in the axial fiber direction
ν_T	Poisson's ratio in the transverse fiber direction
σ	Variance parameter in the GPR
θ	Ply orientation angle
$f(\mathcal{G}_I)$	Function of the mode I energy release rate
J	J-integral results for the energy release rate obtained from Abaqus (2017)
ASTM	American Society for Testing and Materials
BD	Brazilian disk
CFRP	Carbon fiber reinforced polymer
CZM	Cohesive zone model
DCB	Double cantilever beam
ERR	Energy release rate
FE	Finite element
FEA	Finite element analysis
GP	Gaussian process
GPR	Gaussian process regression
GridSearchCV	Hyper-parameters grid search combined with cross validation
ISO	International organization for standardization
KNNR	K-nearest neighbors regression
LEFM	Linear elastic fracture mechanics
LSB	Large-scale fiber bridging
MBT	Modified beam theory
MCC	Modified compliance calibration
MD	Multidirectional
ML	Machine learning
MLR	Machine learning regression

the energy dissipating mechanisms occurring during propagation. These include crack migrations, oscillations, and large-scale fiber bridging (LSB), which may result in specimen toughening.

Failure properties related to delaminations in laminated composites may be determined using either local or global methods. With local methods, the ERR is calculated at discrete locations along the delamination front, based on the local stress and displacement

MMELS	Mixed mode end loaded split
RBF	Radial based function
RFR	Random forest regression
SP	Specimen
UD	Unidirectional
VCCT	Virtual crack closure technique

fields within a defined region of the specimen. In contrast, global methods determine a single representative ERR value for the entire specimen, often using global force and displacement measurements. Often, these failure properties are assessed using a combination of experimental data and numerical simulations [16–18]. The crack driving force or ERR may be determined through simulations employing local techniques like the J-integral [19] or the virtual crack closure technique (VCCT) [20]. In the context of finite element analysis (FEA), the J-integral calculation relies on stress and displacement fields, while VCCT is based on the calculated displacements and nodal point forces. Three-dimensional simulations offer several advantages. They enable the determination of stress and displacement fields, as well as nodal point forces, for intricate designs, allowing for the computation of ERR in complex scenarios. Additionally, three-dimensional simulations facilitate the assessment of ERR along the delamination front. Furthermore, VCCT facilitates mode separation [18], which is essential for addressing the coupling effects between opening, in-plane sliding, and out-of-plane tearing. This is particularly critical when delamination occurs along an interface between two dissimilar plies. One approach to simulate delamination propagation under quasi-static or cyclic applied deformations for determining $\mathcal{G}$ involves creating discrete models of the same specimen with consistent boundary conditions and an increasing delamination length, a [6,7,13,21]. Using this approach, a polynomial function is derived for each tested specimen to establish a correlation between $\mathcal{G}_{FE}$ and a. This function is then applied to experimental data by incorporating the delamination length and applied load at each test point. The resulting data are used to construct an R-curve for quasi-static tests or to calculate the maximum ERR, $\mathcal{G}_{\max}$, for every fatigue test cycle.

In FEAs conducted for composite materials, effective material properties characterize each ply in the model. For example, a UD ply may be described as a transversely isotropic material with five material constants. A plain woven ply may be characterized as a tetragonal material with six material constants. It is crucial to acknowledge that in such intricate material systems, variations in material properties within each ply may occur between batches due to differences in fiber volume fractions or variances in the vacuum applied during manufacturing. These variations may impact the stiffness of the specimen, as well as the stress and displacement fields obtained in the FEAs, resulting in discrepancies in the calculated ERR values. For instance, in Refs. [13,22], the same material, specifically EPR-L20 EPH-960 with T300 carbon fibers, was employed in mode I double cantilever beam (DCB) tests and mixed-mode Brazilian disk (BD) tests, respectively. Despite using the same material, the material properties applied in the FEAs for identical plies in the two investigations differed due to different measured fiber volume fractions.

In previous studies, it was shown that delamination resistance increased as delamination propagated in the context of LSB [23–25]. When numerically analyzing propagating delamination prone to LSB, applying tested material properties or material properties from the literature may not be enough for accurate simulations due to added stiffness as a result of the LSB. Hence, the presence of LSB needs to be accounted for in the analysis [26]. In Ref. [27], FEAs were performed, and the J-integral and cohesive zone model (CZM) were employed to determine the ERR. Based on the results, the fiber bridging reactions under quasi-static delamination propagation within mode I DCB specimens were analyzed. The investigation encompassed various layup configurations, namely $[0_{11}/\theta//0_{12}]$ where the double slash indicates the artificial delamination and $\theta = 0°,\ 30°,\ 45°,\ 90°$. The research revealed that the extent of the bridging phenomenon varies based on the orientation of the interface. Similarly, in Ref. [28], it was demonstrated that the ply layup sequence influenced the R-curve and bridging tractions. This suggests that specific interfaces might display more pronounced and severe fiber-bridging effects than others.

One of the significant challenges in testing UD or MD composite laminates for delamination propagation in fatigue is the vast number of parameters influencing toughness alongside considerable testing noise. These factors complicate the definition of a similitude parameter for determination of failure properties or criteria. A composite laminate is typically affected by changes in the delamination length, load and displacement ratios, lay-up sequence, pre-crack length, etc. [12,29,30]. These parameters may alter the specimen compliance or fatigue resistance. Therefore, when considering the lack of standardized methods for mode I fatigue delamination propagation, it is of great interest to determine which methods are independent of variance and use those to develop failure criteria for design.

In mode I fatigue delamination propagation of composite laminates, the relationship between the rate of delamination propagation da/dN and a function of the mode I ERR $f(\mathcal{G}_I)$ is commonly expressed using the Paris relation [31–33]:

$$\frac{da}{dN} = C f(\mathcal{G}_I)^n \ . \tag{1}$$

In this equation, a represents the delamination length during the test, N is the cycle number, and C and n are fitting parameters. Note that this relation was initially proposed for metals, utilizing the amplitude of the stress intensity factors ΔK as the similitude parameter. For composites, it is common and recommended [34] to use

$$f(\mathcal{G}_I) = \mathcal{G}_{I max} \tag{2}$$

as the similitude parameter. However, additional functions of this parameter may be found in the literature.

In previous investigations, normalization of the fatigue similitude parameter was performed using the quasi-static resistance curve [35–37] to dismiss the influence of the LSB. However, In Ref. [38], a distinction between quasi-static and fatigue-induced LSB was presented. It was shown that the two parameters are different and that the quasi-static resistance curves should not be employed for fatigue data normalization.

In Ref. [30], normalization of the effects of LSB was proposed by deriving a fatigue resistance curve and obtaining the fatigue fracture toughness at no delamination growth G_{IC0}. This was preformed on data from a sequence of fatigue tests performed following the test protocol in Refs. [39,40] for a DCB specimen with increasing pre-crack lengths. Based on the obtained curve, a normalized similitude parameter may be calculated as

$$\Delta\sqrt{\mathcal{G}_{tip}} = \left[\frac{\mathcal{G}_{IC0}}{\mathcal{G}_{IC(a-a_0)}}\Delta\sqrt{\mathcal{G}}\right] \tag{3}$$

where $\mathcal{G}_{tip}$ is the ERR at the delamination tip excluding tractions from LSB and $\mathcal{G}_{IC(a-a_0)}$ is the fatigue fracture toughness for a given delamination extension $a - a_0$, where the delamination extension is defined as the difference between the delamination length a and the initial delamination length a_0. The obtained normalized similitude parameter may then be employed in the Paris relation in Eq. (1).

Another approach focuses on setting an upper limit for design. In Ref. [41], fatigue delamination propagation tests were performed on DCB specimens of seven distinct lay-ups, both UD and MD. It was observed that delamination at a 0°//0° interface exhibited the fastest propagation, or similarly, the least resistance to fatigue delamination, suggesting a potential upper bound for design. Furthermore, in Ref. [42], data from fatigue crack growth tests were experimentally obtained for different load ratios. The study then proposed the Hartman–Schijve equation as a similitude parameter to account for scatter in da/dN vs. $\mathcal{G}_{Imax}$ plots due to varying displacement ratios. In Ref. [43], it was proposed to use the master curve derived by the Hartman–Schijve relation to set an upper bound for design. This was achieved by setting the limit three standard deviations below the parameters obtained from the master curve. The proposed methods may be employed for various cases. However, the definitive correlation between ply layup, bridging tractions, and their collective impact on the ERR has yet to be established.

To validate the accuracy of a FEA, parameters obtained in the analysis, such as load, displacement, compliance, etc., should be compared with those measured in tests. However, suppose the properties used in the analysis do not yield the expected results. In that case, it raises questions about the feasibility of the FEA model used. The influence of inaccurate material properties on the numerically calculated specimen compliance is a critical consideration. This leads to the overarching question: are the material properties from the literature able to model toughening phenomena as LSB sufficiently? Moreover, how much are the ERR values evaluated with J-integral or VCCT influenced by the toughening of the specimens? In order to model the effects of LSB in the finite element (FE) model, one approach may be to model the stiffening caused by LSB as an increase in material stiffness. This may be obtained by calibrating the optimal material properties to match the compliance of the tested specimen. However, this may be a cumbersome process consuming computational time and data.

Use of machine learning (ML) may reduce the need for excessive time-consuming FEAs, as well as complex multidimensional data reduction. In the field of composite laminates, previous works showed great use of ML models for failure prediction [44–48]. For example, in Ref. [49], failure criteria of composite brittle bonded joints were predicted based on VCCT failure parameters. Using a combination of FE VCCT computations and machine learning regression (MLR), the optimal failure parameters were obtained.

In this study, a machine learning method is introduced to calibrate the material properties of each ply in an MD specimen based on the compliance measured in a test. The calibrated properties are then utilized in analyses to determine ERR values from simulations using the local J-integral method. Ultimately, the calibrated properties do not represent the intrinsic properties of the CFRP material system but rather a phenomenological increase in laminate stiffness due to LSB. To showcase the effectiveness of the proposed method, seven different MD layups with initial delamination between two specific plies, oriented either similarly or dissimilarly, and subjected to mode I fatigue testing [29] are considered. Notably, each specimen underwent testing with two initial delamination lengths, potentially influenced differently by LSB [23–25]. Initially, a sensitivity study was conducted to identify the material properties most affecting specimen compliance. Subsequently, three of the most critical properties were selected for calibration. Through automated FEAs and MLR, the specimen compliance obtained from the FE model was calibrated to match the compliance measured in the test. With this approach, the influence of LSB may be quantified and examined as a function of the initial delamination length in the test.

This study aims to suggest a method for obtaining ERR values for delamination propagation within UD or MD laminates due to fatigue loading, given that existing test standards and analytical methods are available only for quasi-static delamination propagation of UD laminates. The results demonstrate that ERR values obtained using the local J-integral [19], along with results from the calibrated simulations, closely align with those calculated using the global modified compliance calibration (MCC) method [1]. Additionally, a comparison between properties calculated for short and long initial delamination lengths shows that the calibrated properties may effectively account for specimen stiffening or changes in material properties between batches.

The manuscript is structured as follows: Section 2 describes the MD specimens tested, including the experimental procedure, setup, and material properties. Section 3 presents the local J-integral and global MCC analysis methods used for evaluating delamination behavior. Section 4 introduces the parametric FE model employed throughout the remainder of the study. In Section 5, a compliance sensitivity analysis is conducted to examine the influence of variations in material properties. Based on this analysis, the three most dominant material parameters are identified. Section 6 then proposes a MLR algorithm for calibrating these mechanical properties in the FE simulation, accounting for stiffness increases due to LSB. Section 7 presents the calibration results, evaluates stiffness variation across different MD interfaces, and compares Paris law curves obtained using both calibrated and uncalibrated properties with results from the global MCC method. Finally, Section 8 summarizes the main findings and contributions of the study.

Table 1
Seven lay-up configurations and interfaces considered with their D_c and B_t parameters [29].

Interface	Layup	B_t	D_c
0°//0°	$[0^\circ_{16}//0^\circ_{16}]$	0	$4 \cdot 10^{-3}$
45°//45°	$[(\pm 45°/0^\circ_{12}/\mp 45°)//(\pm 45°/0^\circ_{12}/\mp 45°)]$	$6 \cdot 10^{-3}$	$8 \cdot 10^{-2}$
90°//90°	$[(0^\circ_{15}/90°)//(90°/0^\circ_{15})]$	0	$4 \cdot 10^{-3}$
0°//45°	$[(0^\circ_{16})//(45°/0^\circ_{16})]$	$3 \cdot 10^{-5}$	$4 \cdot 10^{-3}$
0°//90°	$[(0^\circ_{16})//(90°/0^\circ_{16})]$	0	$4 \cdot 10^{-3}$
45°//−45°	$[(\pm 45°/0^\circ_{12}/\mp 45°)//(\mp 45°/0^\circ_{12}/\pm 45°)]$	0	$8 \cdot 10^{-2}$
30°//−60°	$[(0^\circ_{15}/30°)//(-60°/0^\circ_{15})]$	$2 \cdot 10^{-3}$	$4 \cdot 10^{-3}$

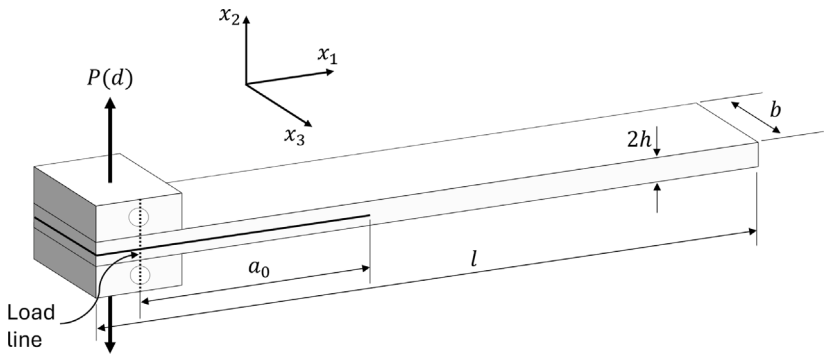

Fig. 1. An illustration of a DCB specimen.

2. Experimental method and materials

In Section 2.1, the material system and layups used, as well as a geometrical description of the specimens, are discussed. Then, a summary of the mode I fatigue test protocol from Ref. [39] is outlined in Section 2.2.

2.1. Material systems and specimen description

In this investigation, DCB specimens composed of an epoxy carbon fiber reinforced polymer (CFRP) material system, namely, M30SC/DT120 (Delta-Preg S.p.A.) were tested for mode I fatigue delamination propagation, and analyzed numerically, as well as with the local J-integral. The numerical results were compared with the tested values, as well as with values obtained with global calculations. The specimens comprised seven different layups, as shown in Table 1. The plies along the delaminated interface are specified in the second column of the table. Note that the double slash indicates the location of the initial artificial delamination.

In laminate theory, the **ABD** matrix is a fundamental concept that characterizes the effective stiffness of a composite laminate [50]. This matrix comprises three 3×3 sub-matrices: **A**, which represents the in-plane extensional stiffness; **B**, which describes the coupling between in-plane and out-of-plane (bending) deformations; and **D**, which captures the bending stiffness of the laminate. When designing a new laminate, two key parameters, D_c and B_t, are often used. These are computed from the D_{ij} components of the **D** matrix as follows:

$$D_c = \frac{D_{12}^2}{D_{11} D_{22}} \quad ; \quad B_t = \frac{D_{16}}{D_{11}} \tag{4}$$

Here, the indices $i = 1, 2, 6$ refer to the longitudinal, transverse, and in-plane shear directions, respectively. In this paper, the longitudinal, transverse, and in-plane shear directions are x_1, x_2, and $x_1 x_3$, respectively, as shown in Fig. 1.

It is desired to maintain $D_c < 0.25$ and $B_t \approx 0$ to minimize the non-uniform distribution of the energy release rate along the delamination front and reduce bending–twisting coupling [51]. The specific values of B_t and D_c calculated for each layup are provided in the third and fourth columns in Table 1.

For each layup, two DCB specimens were tested. Each specimen was tested twice. First, with a short delamination of length between 40 and 70 mm and then with a long propagated delamination between 70 and 120 mm. The fatigue tests are named in the form of SP $\theta_1°//\theta_2°.i.a, b$, where $\theta_1°//\theta_2°$ represents the interface layup, as listed in Table 1, $i = 1,2$ represents the specimen number, and the parameters a, and b represent the first and second fatigue runs, respectively. For example, SP 45°//45° 1.b represents the first specimen of the 45°//45° layup on the second fatigue run. A total of 28 tests were conducted, namely, seven interfaces with two specimens examined for each interface, and two initial delamination lengths tested for each specimen. Due to data acquisition issues for SP 0°//0° 1.a, the results from this test were dismissed. Hence, only 27 fatigue tests are presented in this study.

A three-dimensional illustration of a DCB specimen is presented in Fig. 1. All specimens had approximate dimensions of $l = 200$ mm in length, $2h = 5.2$ mm in thickness, and $b = 25$ mm in width, as presented in the figure. An artificial delamination with length $a_0 \approx 50$ mm, measured from the load line, was intentionally introduced between the specified plies in each layup.

Table 2
Material properties of M120SC/DT120 [52].

Properties	E_A (GPa)	E_T (GPa)	ν_A	ν_T	G_A (GPa)
M120SC/DT120	155	7.8	0.27	0.022	5.5

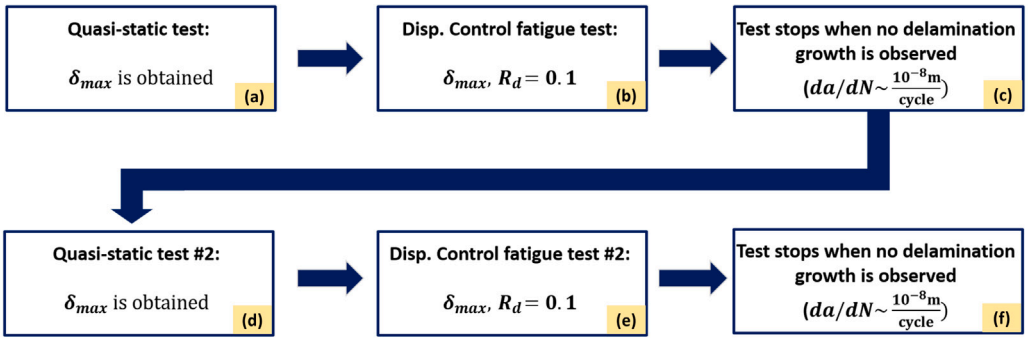

Fig. 2. A flow chart illustrating the stages of testing conducted for each specimen in accordance with Ref. [39].

A homogenized UD composite ply may be considered transversely isotropic. Therefore, it may be described by five independent material properties: E_A, E_T, ν_A, ν_T, and G_A, where the indices A and T represent the axial and transverse fiber direction. Here, E is Young's modulus, ν is Poisson's ratio, and G is the shear modulus. Note that the sixth mechanical property G_T is a function of the other parameters and may be calculated as:

$$G_T = \frac{E_T}{2(1+\nu_T)} \tag{5}$$

The material properties initially used in the FEAs were obtained from Ref. [52] and are presented in Table 2. The transverse shear modulus G_T was corrected and calculated according to the transversely isotropic relation in Eq. (5). The value obtained for this parameter is $G_T = 3.81$ GPa.

2.2. Test protocol

The specimens of the seven layups in Table 1 underwent mode I fatigue testing following the protocol outlined in Ref. [39]. Additional test details are available in Refs. [29,41]. For clarity, a concise description of the test protocol is provided here, and the procedural steps are illustrated in Fig. 2.

According to Ref. [39], the length l, thickness $2h$, width b, and the initial delamination length a_0 of each DCB specimen were measured. Each specimen underwent four loading stages. In the first stage (Fig. 2.a), quasi-static deformation following Ref. [53] was performed to initiate a precrack from the artificial delamination. From this test stage, the maximum displacement δ_{max}, which is the final mode I opening value measured before delamination propagation was observed, was determined.

The second stage (Fig. 2.b) included tensile mode I cyclic fatigue opening displacements. The displacement ratio R_d, defined as

$$R_d = \frac{\delta_{min}}{\delta_{max}} \tag{6}$$

where δ_{min} and δ_{max} are the minimum and maximum displacements, respectively, was chosen to be 0.1. Note that this ratio and the test frequency remained constant throughout the test. During the test, the minimum and maximum loads P_{min} and P_{max} were measured for each cycle. Note that the load ratio R_P, defined as

$$R_P = \frac{P_{min}}{P_{max}} \tag{7}$$

is required to remain within an error of 10% of R_d throughout the entire test.

When the propagation rate fell below 10^{-8} m/cycle, the second stage of the test was halted (Fig. 2.c). The process was repeated by generating a new pre-crack through quasi-static loading (Fig. 2.d). Subsequently, the following step (Fig. 2.e) included cyclic fatigue deformations again with a displacement ratio $R_d = 0.1$. Again, the fatigue test was completed once delamination propagation rate reached a value of approximately da/dN 10^{-8} m/cycle (Fig. 2.f). Consequently, each specimen underwent two fatigue tests: first, with a short delamination of length between 40 and 70 mm and then with a long propagated delamination between 70 and 120 mm.

Additionally, during the test, each specimen was photographed from both sides and after completion, the delamination lengths a were measured from the load line, shown in Fig. 1, to the delamination front. The delamination lengths were measured with correspondence to the cycle number.

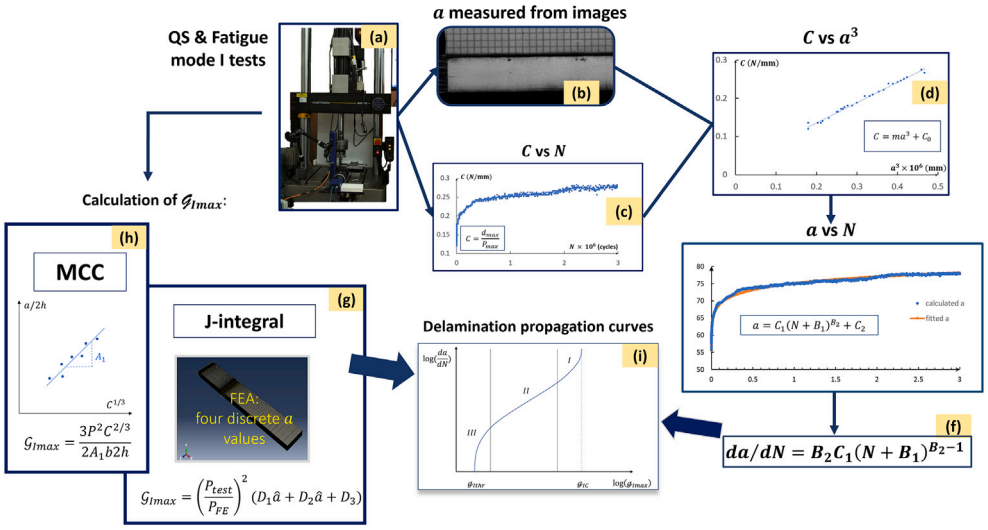

Fig. 3. Flow chart of the analysis methodology.

3. Analysis methods

In this Section, the analysis methods used in this study are described. In Sections 3.1 and 3.2, the computational analysis performed to determine the required values of da/dN and $\mathcal{G}_{I max}$, are described, respectively. The obtained delamination propagation rate da/dN and $\mathcal{G}_{I max}$ values are plotted on a log–log scale, as demonstrated in Fig. 3.i based on the Paris relation in Eq. (1). In Fig. 3, a flow chart illustrating the analysis procedure for determining the Paris plot for each tested specimen is presented. The right side of the figure refers to the method employed to determine the delamination propagation rate da/dN, as described in Section 3.1. The left side is related to the computation of $\mathcal{G}_{I max}$ using the MCC method or the J-integral in conjunction with FEA results, as explained in Section 3.2.

3.1. Delamination propagation rate

The fatigue DCB specimens tested in Ref. [29] were photographed during each test. An example of an image used for delamination length measurements a is presented in Fig. 3.b. These measurements were taken at predefined intervals. Through machine readings, the cycle number N, maximum and minimum applied loads $P_{\max}$ and $P_{\min}$, respectively, and maximum and minimum displacements $\delta_{\max}$ and $\delta_{\min}$, respectively, are also obtained.

The compliance value at each cycle was calculated as

$$C = \frac{\delta_{\max}}{P_{\max}} \,. \tag{8}$$

Then, incremental compliance values C were plotted against the corresponding cycle number N as demonstrated in Fig. 3.c. The compliance values C at specific intervals N, where the delamination lengths a were measured, were plotted against the measured a values, as demonstrated in Fig. 3.d. A linear curve of the form

$$C = ma^3 + C_0 \tag{9}$$

was fit through the data to determine the slope and intercept, m and C_0, respectively. Note that Eq. (9) may also be expressed as

$$a = \sqrt[3]{\frac{C - C_0}{m}} \tag{10}$$

to enable continuous evaluation of a as a function of the compliance C throughout the entire test duration.

The calculated a values are plotted against the cycle numbers N, as shown in Fig. 3.e, and a relation of the form

$$a = C_1(N + B_1)^{B_2} + C_2 \tag{11}$$

may be applied to the resulting curve. In Eq. (11), C_i and B_i $(i = 1, 2)$ are fitting parameters. The delamination propagation rate is then determined by taking the derivative of Eq. (11) with respect to N to obtain

$$\frac{da}{dN} = B_2C_1(N + B_1)^{B_2-1} \,. \tag{12}$$

as depicted in Fig. 3.f. This equation provides the delamination extension rate da/dN for every cycle N.

3.2. Mode I energy release rate

The energy release rate $\mathcal{G}_{Imax}$ values may be obtained using various methods. Among these are standardized global calculation methods, such as the MCC or modified beam theory (MBT) from the mode I quasi-static test standards [1,53]. Or local calculation methods such as the J-integral or VCCT which are often used with numerical FEA results. Note that with the local methods, when using three-dimensional models, mode separation is enabled, and the behavior of $\mathcal{G}_{Imax}$ along the delamination front may be evaluated. However, for validation of the material properties used in the simulations is of great importance.

In this study, both the global MCC method and the local J-integral were employed and compared. In Section 3.2.1, the MCC method is presented. The methodology used for the determination of $\mathcal{G}_{Imax}$ with the J-integral in conjunction with FEA results is described in Section 3.2.2.

3.2.1. Modified Compliance Calibration (MCC) — global analysis method

The MCC is a standard global method [1,53] used for calculation of the ERR values for DCB mode I quasi-static tests using the expression

$$\mathcal{G}_I = \frac{3P^2C^{2/3}}{2A_1 b(2h)} \quad . \tag{13}$$

In Eq. (13), P is the applied load, C is the compliance of the specimen, b is the specimen width, and $2h$ is the specimen thickness, illustrated in Fig. 1. The parameter A_1 represents the slope between the delamination length a normalized by the specimen thickness $2h$, as demonstrated in Fig. 3.h.

The MCC method may also be used to determine the maximum ERR values in every fatigue cycle in a mode I DCB fatigue test. In the case of a fatigue test, the compliance C in Eq. (13) is obtained from Eq. (8) for a specific cycle N.

Values of $\mathcal{G}_{Imax}$ are then obtained from Eq. (13) by substituting the load P with the maximum load $P_{\max}$ measured in every cycle and with values of a calculated from Eq. (11) for every cycle.

3.2.2. Numerical J-integral — local analysis method

The J-integral is a path-independent contour integral used to determine the energy release rate value. It was demonstrated in Ref. [19] that under small scale yielding conditions, the value of the J-integral is equal to the energy release rate, namely, $\mathcal{G} = J$. This study follows local analysis methodologies employed in Refs. [6,7,13]. These analysis methods, incorporating the J-integral, were demonstrated for nearly mode I fatigue analyses, as well as for nearly mode II, and mixed-mode to obtain the quasi-static resistance curves for MD composites. For completeness, the analysis stages are summarized here.

Finite element simulations were conducted at four different delamination length values, namely a_{1FE}, a_{2FE}, a_{3FE}, and a_{4FE}. The span of the analyzed a values must meet the condition

$$a_{1FE} < a_0 \quad ; \quad a_f < a_{4FE} \tag{14}$$

where a_0 and a_f are the initial and final delamination lengths during the experiments, as measured from the load line. By doing so, the analyses cover the range of delamination lengths in the test. For all four analyses, the load assigned in the FE model was constant at $P = 20$ N.

The stress and displacement fields were obtained for each analysis and used to calculate the maximum ERR in every cycle. Results of $\mathcal{G}_{IFE}$ were calculated using the J-integral Abaqus calculation [54]. Values were obtained through the width of each modeled delamination length for each specimen. To obtain a single ERR value, the integrated average was calculated as

$$\bar{\mathcal{G}}_{IFE} = \frac{1}{b} \int_0^b \mathcal{G}_{IFE}(x_3)\, dx_3 \tag{15}$$

where x_3 is the direction aligned with the width b, shown in Fig. 1. Based on the results obtained for each specimen, a polynomial fit of the form

$$\bar{\mathcal{G}}_{IFE}(\hat{a}) = D_1\hat{a}^2 + D_2\hat{a} + D_3 \tag{16}$$

was fit through the numerical data. In Eq. (16), $\bar{\mathcal{G}}_{IFE}(\hat{a})$ is the continuous integrated mean ERR value related to the load P_{FE} which was employed in the FE simulations, as a function of the normalized delamination length $\hat{a}$ calculated as $\hat{a} = a/a_0$ where a_0 is the artificial delamination length measured from the load line. The parameters D_i, $i = 1, 2, 3$ in Eq. (16) are fitting parameters. Next, a calculation of the form

$$\mathcal{G}_{Itest} = \left(\frac{P_{test}}{P_{FE}}\right)^2 \bar{\mathcal{G}}_{IFE}(\hat{a}) \tag{17}$$

was performed to obtain values of $\mathcal{G}_{Imax}$ throughout the test by substituting P_{test} values, namely, the maximum loads measured in each cycle throughout the test. The parameter P_{FE} is the load employed in the FE simulations, and $\bar{\mathcal{G}}_{IFE}(\hat{a})$ was obtained from Eq. (16).

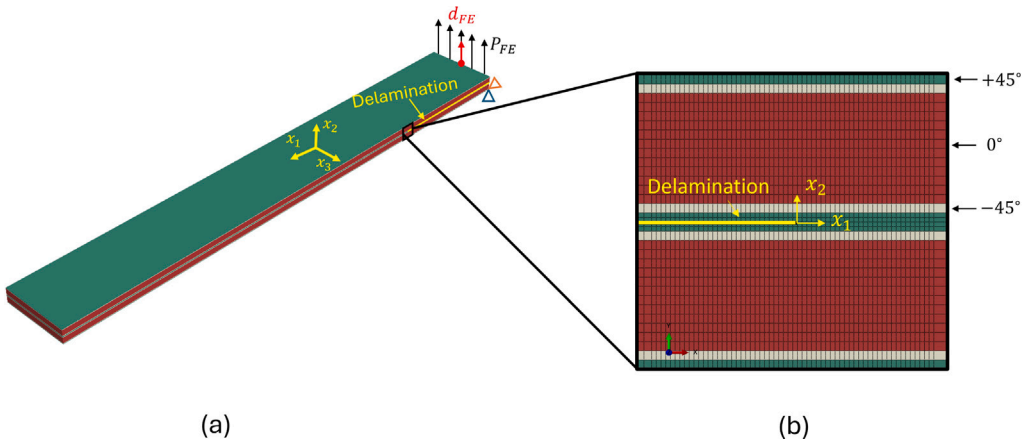

Fig. 4. Example of an FE DCB model, with an initial delamination between two UD plies with fibers oriented in the 45°-direction. (a) Overall view of the DCB FE model, the applied load is marked with black arrows, and the orange and blue triangles represent constraints in the x_2 and x_3 directions, respectively. (b) A two-dimensional focused view of the delamination tip: Plies oriented in the 45° and −45° directions are in green and gray, respectively; plies in the 0°-direction are in red.

4. Finite element model

A three-dimensional parametric anisotropic FE DCB model was designed in Abaqus [54]. The model was programmed with Abaqus Python scripting to enable parametric flexibility in geometric specimen dimensions, material properties, as well as applied boundary conditions. The parametric design included the specimen length L, thickness $2h$, width b, and delamination length a, illustrated in Fig. 1. The material properties are defined as engineering constants in the FE model. Nine parameters are employed in the Python code, namely, $E_1, E_2, E_3, \nu_{12}, \nu_{13}, \nu_{23}, G_{12}, G_{13}$, and G_{23}, where the notations $1, 2$, and 3 represent the x_1, x_2, and x_3 directions shown in Fig. 4. In addition, the layup of the model, including the number of plies, as well as the thickness and orientation of each ply, are determined using specified parameters in the Python code. This enables automatic FE model building for varying layups and specimen dimensions. Additionally, the load applied in each simulation P_{FE} is also parameterized. Finally, a delamination of length a is introduced as a crack on the midplane.

The mesh density is also defined through the Python code, with the number of mesh elements generated accordingly. The elements adjacent to the delamination tip are configured as quarter-point elements. The elements in the delamination tip region are designed to have an aspect ratio of 1×1 in the x_1 and x_2 directions. In addition, the mesh density is biased both in the x_1 and in the x_2 towards the delamination tip. This was done so that the number of elements is reduced without compromising computational accuracy, consequently reducing computation time. Such a parametric three-dimensional model enables numerous simulations with varying parameters for each simulation.

In this study, the parameters used in the model were defined based on the specimens tested in Ref. [29]. These specimens included 32 plies, modeled as 32 cells. Each ply was set as a homogeneous elastic solid. Since all plies used in the current study are UD, each ply is considered transversely isotropic and characterized using the five required material properties out of the nine used in the general case of an orthotropic material. The properties were defined in the axial and transverse directions with respect to the fiber orientation. The global orientation of each modeled ply, shown in Fig. 1, was set in the model script, and the material properties used in the axial and transverse directions of the ply were rotated accordingly by Abaqus [54].

In Fig. 4.a, an example of a three-dimensional DCB model is shown. It may be noted that half of the load block, close to the free specimen edge, is omitted in the FE model. Hence, in the figure, the model starts at the load line, marked in Fig. 1. In Fig. 4.b, a close-up view of a specimen with a crack along the 45°//45° interface is presented. The layup for this interface is described in Table 1. In the figure, plies oriented in the 45° and −45° directions are in green and gray, respectively, and plies in the 0° direction are in red. The load is applied to the upper DCB arm, as shown in Fig. 4.a. To obtain a constant load along the load line, the lower arm is held in the x_2 and x_3 directions as represented in Fig. 4.a by the blue and orange triangles. Note that the load was distributed as recommended in Ref. [13].

A convergence study based on the calculated ERR was performed to find the optimal element number and size. Based on the results from this study, the chosen model mesh included 351,900 20-node brick elements with 1,486,727 nodes. Through the width direction of the model (x_3 in Fig. 4), there were fifty elements, resulting in a width of $B = 0.5$ mm for each element. Note that the length of each element in the x_1 and x_2 directions in Fig. 4, near the delamination front, was $a = 0.1625$ mm, resulting in a width-to-length ratio of $B/a \approx 3$. This ratio was found to be sufficient and convergence was achieved.

Additionally, to validate the calculations made, path independence of the J-integral was examined across six contours. the contours used are illustrated in Fig. 5, where each domain includes an added strip of elements surrounding the delamination. The results showed that the differences among the third to sixth contours were less than 0.001%. Based on these findings, the fourth contour was selected and used for the remaining analyses.

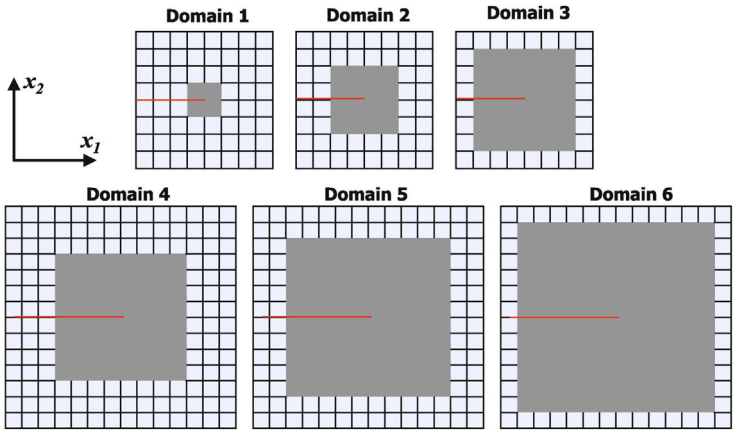

Fig. 5. Integration contours for the J-integral, with the red line indicating the delamination. *Source:* Reproduced from [55].

5. Compliance sensitivity

In this study, the stress and displacement fields obtained from numerical FEAs were used with the J-integral local approach to determine $\mathcal{G}_{I\,max}$. In such a case or in any case that FEA results are used for the evaluation of physical constants, it is crucial to verify the accuracy of the FEA model. One way to do this is to examine the differences between the compliance obtained from a test with those calculated from the FEA. In this study, the FE model described in Section 4 was validated using this compliance comparison approach. First, a compliance sensitivity study was performed to get a sense of the significance of each mechanical property defined in the FE model on the compliance of the specimen. As explained in Section 2.1, a UD ply may be homogenized and described with five independent material properties, namely E_A, E_T, ν_A, ν_T, and G_A. The sixth material property, G_T, is calculated using Eq. (5). The relationship between these five material constants in a DCB specimen and the numerical compliance obtained was examined with a variable significance test. Based on the obtained results, in this section, the material properties with the most effect on compliance are discussed.

An FE DCB model was designed for the significance test using the parametric model described in Section 4 with a delamination length of $a = 50$ mm and a load of $P = 50$ N. Each material property in the axial and transverse orientations of the fibers within the ply was independently changed in each FEA in a range of $k = [-30\%, -15\%, 0\%, 15\%, 30\%]$ of the original property, which was obtained from the literature [52] and given in Table 2. To account for the various fiber orientations, this test was repeated for three different interfaces, namely, 0°//0°, 45°//45°, and 0°//90°, with the layups given in Table 1.

For each FEA with each material property within the examined range, the compliance was computed. To estimate the significance of each material property on the compliance, the relative difference between the compliance values obtained from the model with the original literature properties and that obtained from an FE model with a changed property was calculated as

$$\Delta C^{FE} = \frac{C_k^{FE} - C_0^{FE}}{C_0^{FE}} \cdot 100\% \tag{18}$$

where C_0^{FE} is the compliance obtained from the base FE model with the material properties from the literature, given in Table 2, and C_k^{FE} is the compliance obtained for the same model with a change of $k\%$ for a single property. A total of 63 FEAs were performed, with 21 conducted for each of the three interfaces examined. Five properties were analyzed for each interface, with four different values tested for each property and a single run with properties form the literature for each interface. In Fig. 6, the relation between the change in compliance ΔC^{FE} as a function of the change of each material property is presented for each layup. From the obtained plots, a polynomial relation between each property and the compliance was observed.

The results for each property change of $k = +30\%$ are presented in Table 3 for each layup. It may be observed that the most effect on compliance, namely the largest values for ΔC^{FE}, ranged between 19% to 20% for $E_A + 30\%$. The next most significant difference in compliance was related to $G_A + 30\%$ and ranged between 2.2% through 4%. Then, influence of $E_T + 30\%$ was almost negligible and ranged between 0.59% for the 0°//0° interface to 1.1% for the 45°//45° interface. It may be noted that a negligible difference in the compliance was obtained for $\nu_A + 30\%$ and for $\nu_T + 30\%$ and ranged between 0.08% through 0.15% for the former and between 0.001% through 0.003% for the latter. From the sensitivity study performed, it may be concluded that E_A, G_A, and E_T, in decreasing order of impact, are the material properties that exert the most influence on specimen compliance tested in mode I. From a physical standpoint, this conclusion is expected since data was obtained from mode I testing, which is mostly governed by properties in the axial direction (x_1 in Fig. 1).

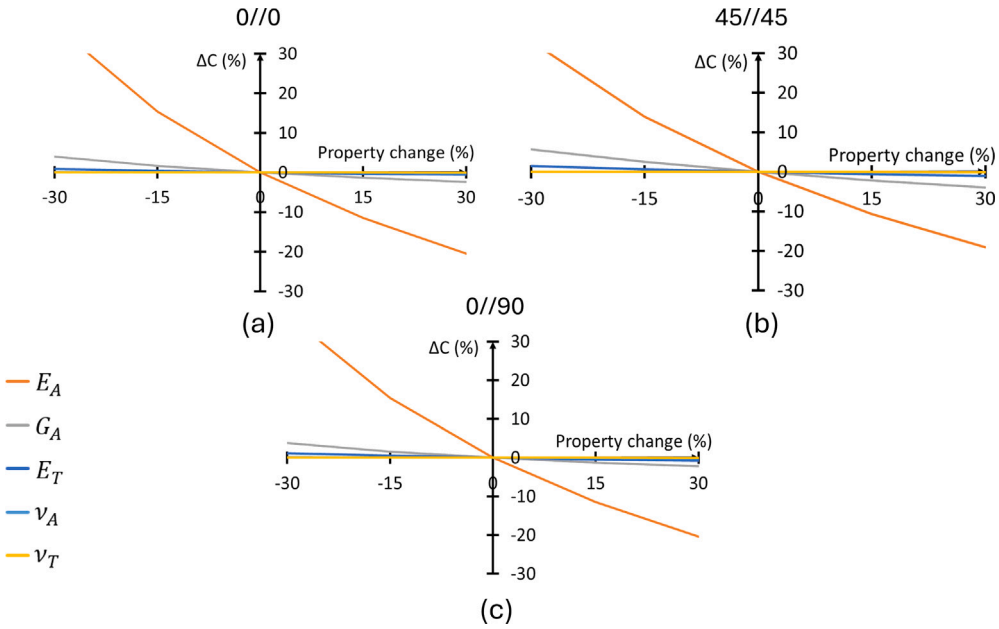

Fig. 6. The change in compliance ΔC^{FE} % with respect to a change in the material properties from the literature for (a) 0°//0° layup, (b) 45°//45° layup, and (c) 0°//90° layup.

Table 3
The change in the compliance obtained from FEA ΔC^{FE} given in Eq. (18) due to a 30% increase of each MP.

Interface	ΔC^{FE} %		
	0°//0°	45°//45°	0°//90°
E_A+30%	20.0	19.0	20.0
G_A+30%	2.4	4.0	2.2
E_T+30%	0.59	1.10	0.80
ν_A+30%	0.15	0.08	0.18
ν_T+30%	0.001	0.004	0.003

6. Compliance calibration algorithm

The FE model described in Section 4 was validated against test data using the material properties from the literature shown in Table 2. The validation of the 0°//0° layup FE model yielded good consistency with the test specimen with a relative difference of 3.7% between the compliance measured in the test and that calculated in the FEA. This result suggests that the FE model is valid. However, for the additional layups tested, this validation test resulted in large disparities of more than 52.2% between the compliance of the FE models and the compliance of the test specimen. These differences may be related to LSB, which are known to be more pronounced in 0°//45°, 0°//90°, 45°//−45° or 90°//90° interfaces compared to a 0°//0° interface [27,28]. To account for LSB, it is necessary to incorporate this toughening mechanism, which influences the model stiffness differently depending on the ply orientations, into the FE model. Additionally, note that variations in material properties across different batches may also occur due to manufacturing-related differences and should also be considered in the material properties used in the FE models.

To account for LSB and calibrate the FE models for all seven layups, the approach employed in this study was to minimize the disparities between the compliance of the tested specimens and that of the FE model by calibrating the material properties that were found in Section 5 to most influence the compliance. Calibration is achieved by accounting for the stiffening effect caused by LSB an increase in the mechanical properties of the sample [26].

The calibration of material properties is expressed as an optimization challenge and follows a structured process involving iterative automated FEAs coupled with predictions from an MLR model. A flowchart of the calibration algorithm is presented in Fig. 7. The process begins by defining the lower and upper limits of three material properties that were found to have the most influence on compliance in Section 5, namely, E_A, E_T, and G_A. This step is shown in Fig. 7.a. The boundaries were chosen to be within ±30% of the original values obtained from the literature and shown in Table 2. For each examined material property, within the chosen boundaries, five values were used. Then, these fifteen values, namely, five values for each material property with three material properties, are sorted into all possible combinations, resulting in 125 different sets of material properties.

For each tested specimen, 125 FEAs were performed; one for every set of properties from the 125 combinations (Fig. 7.b). For this task, the FE model described in Section 4 was used with the load P and the related delamination length a values chosen from the results of the fatigue tests.

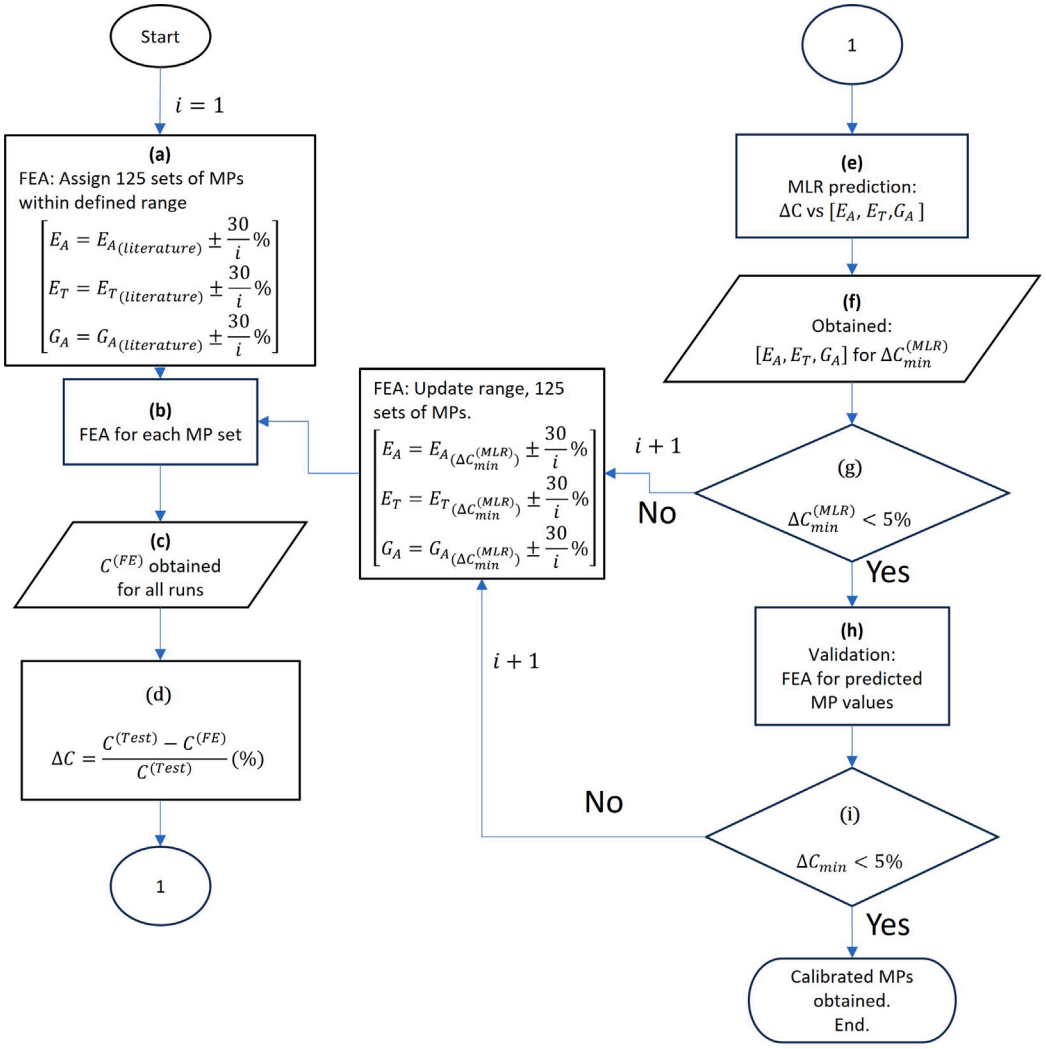

Fig. 7. A flowchart describing the material property calibration process.

Table 4
The difference in compliance ΔC (%) calculated with Eq. (8) between the compliance obtained from the test and the compliance obtained from the FEA using the calibrated properties for four different interfaces with short delamination length for various cycles N.

Specimen	$N = 100$	$N = 500$	$N = 1000$	$N = 9000$	$N = 28000$	$N = 248000$
SP 0//0 2.a	−3.5%	1.2%	−1.2%	3.5%	5.3%	1.2%
SP 0//90 1.a	−4.1%	−3.5%	−0.9%	6.5%	−4.2%	−2.2%
SP 30//−60 1.a	1.8%	−1.6 %	−2.7%	6.2%	2.3%	−3.3%
SP 0//45 1.a	0.8%	−1.8%	1.0%	−7.6%	−3.7%	−5.4%

To choose a uniform reference point for all properties calibration for all specimens, the degree of LSB-induced stiffening increase during a fatigue test was examined. Notably, reports in the literature indicate that LSB is primarily generated under quasi-static delamination propagation [38]. To evaluate the changes in stiffness throughout the test, the difference between the compliance measured from the test data was compared with that evaluated with the FE model using Eq. (19) at N = 100, 500, 1000, 9000, 28 000, 248 000 cycles. In Table 4, results are presented for four specimens with short initial delaminations, each corresponding to a distinct interface layup, namely 0°//0°, 0°//90°, 30°// − 60°, and 0°//45°. The results show small fluctuations, with less than a 10% difference between the measured and simulated stiffness at various points throughout the test. Given the relatively small magnitude of these fluctuations, any consistent reference point could, in principle, be used for calibration. However, during the initial loading cycles — prior to the onset of stable Stage II delamination propagation — extreme values of da/dN and irregular machine load readings may occur, potentially compromising calibration accuracy, as illustrated in Fig. 3.i. To avoid these transient effects and ensure consistency, N = 1000 cycles was selected as the standard reference point for all calibrations across all specimens and tests.

Additionally, all geometric features in the FE model are specified with respect to the examined specimen. From the analyses, the compliance obtained from the FE model, namely, C^{FE}, is calculated using Eq. (8) with P taken as the load applied in the FE model, namely the load at $N = 1000$ from the test, and δ as the related opening mode I displacement obtained in the FEA (Fig. 7.c). The relative difference between the compliance of the specimen from the fatigue test results and that from the FEA was then calculated as

$$\Delta C = \frac{C^{Test} - C^{FE}}{C^{Test}} \cdot 100\ \% \tag{19}$$

where ΔC is the difference in % and C^{Test} is the compliance calculated with Eq. (8) for P and δ obtained from the test data for $N = 1000$ (Fig. 7.d).

The model is trained to fit a three-dimensional manifold through the obtained ΔC values with respect to the corresponding sets of the significant material properties, namely, E_A, E_T, and G_A. Then, using the obtained relations, the difference in compliance ΔC may be predicted for any given set of material properties (Fig. 7.e). Based on this regression, the combination of the material properties corresponding to the minimal difference in compliance ΔC_{min} is obtained (Fig. 7.f). The value of the best result obtained from the regression model is then examined so that it would meet the requirement of $\Delta C_{min}^{MLR} \leq 5\%$ (Fig. 7.g). If not, the algorithm is repeated with updated upper and lower bounds of ±15% from the predicted material properties in the current iteration. This step is performed in order to increase the search resolution around the current optimum, increasing the probability of satisfying the required stopping criterion. If the requirement is met, the calibrated material properties are then validated in the FE model by performing analysis with the calibrated material properties predicted from the regression model (Fig. 7.h). If the compliance obtained from the FEA satisfies the requirement of $\Delta C_{min} \leq 5\%$ (Fig. 7.i), the calibrated material properties are determined.

Several MLR models available in `scikit-learn` [56] were investigated for this task, namely Gaussian process regression (GPR), random forest regression (RFR), and K-nearest neighbors regression (KNNR). To determine which algorithm is most suitable, predictions for SP 0°//0° 2.a and SP 45°//45° 1.a were examined following the procedure presented here. Each MLR model was then trained to find the relationship between the material properties and the compliance difference, eventually predicting ΔC_{min}^{MLR}. For this, 80% of the data, namely, input material properties and obtained ΔC values, was used for training and the remaining 20% for testing.

It was found that the RFR model did not generate a continuous surface, as the predicted points were staggered in clusters with relatively poor accuracy. In contrast, the KNNR and GPR models both generated continuous surfaces that could characterize the physical relationship between material properties and compliance. Nevertheless, the GPR model proved to be the most efficient in terms of computational time and complexity. For this reason, the GPR model was selected for the calibration algorithm in this study.

The GPR model is a non-parametric and probabilistic machine learning technique used for regression tasks [57]. The GPR defines the relations between the different inputs based on a covariance function, also known as the kernel. The kernel used in this model is the radial basis function (RBF), which assumes that two points with close inputs will yield close outputs. The RBF may be given as

$$K(x_i, x_j) = \sigma^2 \exp\left(-\frac{\|x_i - x_j\|^2}{2\hat{l}^2}\right) \tag{20}$$

where σ is the variance, x_i and x_j are close input points, and $\hat{l}$ is the length parameter controlling the amplitude of the relation between adjacent points.

In all subsequent applications of the GPR, an 80/20% train-test split was employed. Additionally, a grid search combined with a cross-validation (`GridSearchCV`) framework was utilized to fine-tune the hyperparameters of the model, thereby ensuring an optimal fit to the data.

To reduce computational time, several measures were implemented. First, after calibrating a specimen of a certain layup and delamination length, when calibrating the second specimen of the same layup, it is expected that they will show similar behavior since they share the same layup and approximately similar delamination lengths. Based on that notion, the number of FEA runs performed was reduced. This reduction was achieved by setting the initial point of the searching boundaries for each property as the calibrated properties obtained for the already calibrated specimen of the same layup, then the probability of being closer to the optimum is higher, reducing the number of required iterations. Moreover, the search span was reduced to ±15% of the initial point with three linearly spaced values, instead of 125 required FEAs as was done for the first specimen calibration. This search span reduction resulted in 27 required FEAs.

Secondly, for the calibration of the same specimen during the second stage of testing, which involves a longer delamination length, the relative difference between the compliance values measured in the first and second stages of the test at cycle $N = 1000$ was calculated. The material properties from the first stage were then adjusted linearly by a factor of this relative difference in compliance to provide a rough estimate for the optimal properties in the second stage. Subsequently, a regression of E_A, G_A, and E_T was generated using GPR with three linearly spaced values within the span of ±15% about the adjusted properties. This approach also resulted in 27 FEAs instead of 125.

7. Results and discussion

In this section, all results are presented. In Section 7.1, the resulting calibrated material properties for the layups in Table 1 are presented. Note that the calibrated values were obtained according to the procedure described in Section 6. Furthermore, all material properties were obtained in the local ply orientation, namely, in the fiber axial and transverse orientations.

Table 5
Material properties E_A, E_T and G_A calibrated using the procedure in Section 6 with respect to cycle $N = 1000$. The parameter ΔC is calculated using Eq. (19).

Layup	a ($N = 1000$) (mm)	E_A (GPa)	E_T (GPa)	G_A (GPa)	G_T (GPa)	ΔC_{min} ($N = 1000$) (%)
0//0 1.b	110.3	198.2	8.2	5.4	4.0	−1.9
0//0 2.a	52.5	161.6	7.8	6.9	3.8	−1.2
0//0 2.b	118.5	189.7	9.1	5.1	3.8	2.3
45//45 1.a	48.3	181.8	7.8	4.6	3.8	3.2
45//45 1.b	99.8	196.4	8.7	5.6	3.9	−0.1
45//45 2.a	48.7	190.7	8.3	5.0	4.1	−0.2
45//45 2.b	78.0	198.4	8.7	5.7	4.3	0.5
90//90 1.a	61.2	306.6	11.9	10.5	5.8	−0.6
90//90 1.b	102.7	291.8	11.4	10.0	5.6	1.5
90//90 2.a	63.0	243.2	9.5	8.3	4.6	1.1
90//90 2.b	82.7	260.1	10.1	8.9	5.0	−1.0
0//45 1.a	50.3	242.6	9.5	8.7	4.6	1.0
0//45 1.b	81.3	254.7	9.5	8.9	4.6	−3.9
0//45 2.a	50.3	171.6	7.7	7.0	3.8	1.9
0//45 2.b	78.0	218.4	9.7	9.3	4.8	−2.0
0//90 1.a	59.1	211.5	10.1	6.1	4.6	−0.9
0//90 1.b	88.9	247.9	12.1	7.7	10.0	−1.8
0//90 2.a	59.7	236.9	11.0	7.3	5.4	−2.4
0//90 2.b	78.8	251.4	13.8	7.8	10.1	−3.5
45//−45 1.a	63.1	210.8	8.2	7.2	4.0	0.4
45//−45 1.b	73.3	210.9	8.6	7.5	4.2	−0.7
45//−45 2.a	64.4	210.9	8.1	7.2	4.0	1.2
45//−45 2.b	84.5	213.0	9.0	7.6	4.4	−1.6
30//−60 1.a	67.7	211.5	8.2	7.3	4.0	−2.8
30//−60 1.b	93.0	228.4	9.1	7.8	4.4	1.4
30//−60 2.a	65.7	207.2	8.2	7.4	4.0	−1.8
30//−60 2.b	82.5	211.5	8.2	7.3	4.0	0.8

For each chosen set of properties, values of $\mathcal{G}_{I\,max}$ were calculated via local FEA J-integral computations following the methodology described in Section 3.2.2. In Section 7.2, the resulting Paris plots obtained for each interface, specimen, and initial delamination length, using the local J-integral approach with calibrated and literature properties are presented and compared with the Paris plots obtained with the global MCC method.

7.1. Calibrated material properties

The procedure described in Section 6 was employed for each tested specimen for the short and long delamination lengths for all interfaces. Calibration was performed with respect to the $N = 1000$ cycle of the fatigue test. The calibrated properties E_A, E_T, and G_A were chosen from the calibration algorithm for the smallest ΔC^{FE}, which indicates the best compliance match to that obtained in the test. The parameter G_T was calculated for the chosen properties according to Eq. (5).

The obtained calibrated properties for each specimen are presented in Table 5. Note that some values fall outside the expected physical boundaries for this material. This is due to the fact that the obtained properties are a combination of the material's stiffness and the additional stiffness introduced by the LSB. In the first column, the interface, specimen, and test details are specified. The second column provides the initial delamination length for each specimen. Columns three through five list the values obtained for E_A, E_T, and G_A. Column six presents the values for G_T, which were calculated using Eq. (5) based on the calibrated E_T values. Finally, the last column shows the percent difference between the FE compliance and the compliance measured in the test, calculated using Eq. (19).

To visualize the obtained calibrated properties, stacked column plots of E_A, E_T, and G_A are presented in Figs. 8 through 10, respectively. In the figures, the calibrated properties for each interface are presented. Two specimens were tested for each interface, denoted in blue and orange, and labeled as $\theta_1°//\theta_2°.i.a, b$, where $\theta_1°$ and $\theta_2°$ represent the fiber orientations in the upper and lower plies, respectively, relative to the x_1-axis shown in Fig. 4. The index i is used to indicate the specimen number, with $i = 1$ or 2 as shown in the figure legend. Parameters a and b represent the first and second fatigure runs, respectively. Properties for specimens with a short initial delamination (1.a and 2.a) are shown in light blue and light orange, respectively. Darker shades indicate specimens with longer initial delaminations (1.b and 2.b). Recall that the calibrated material properties for SP 0°//0° 1.a are dismissed since data acquisition was not performed properly and some values were missing. It can be observed from the figures that an increase in the calibrated material properties occurs with longer delamination lengths for all specimens and interfaces, except for the 90°//90° interface. This is discussed in the sequel.

To better understand the influence of LSB on specimen stiffness and LSB relation to the initial delamination length, namely, short and long test stages for all interfaces and layups tested from the obtained calibrated properties shown in Table 5 and Figs. 8 through 10, two comparisons were made considering the calibrated material properties E_A, E_T, and G_A given in Table 5. The

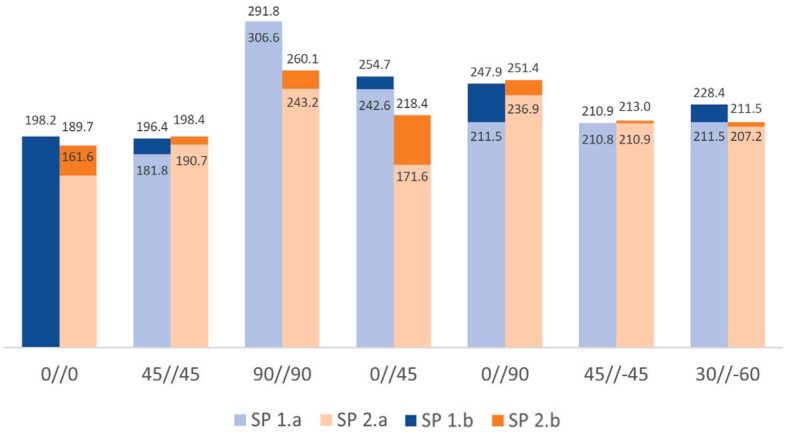

Fig. 8. The calibrated values for E_A (GPa).

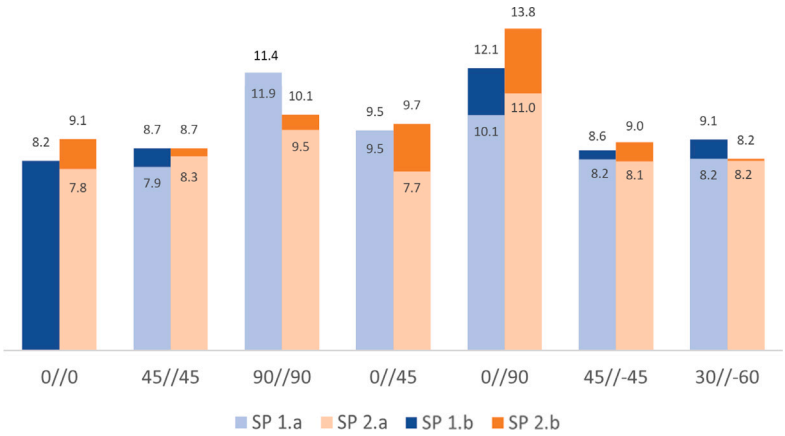

Fig. 9. The calibrated values for E_T (GPa).

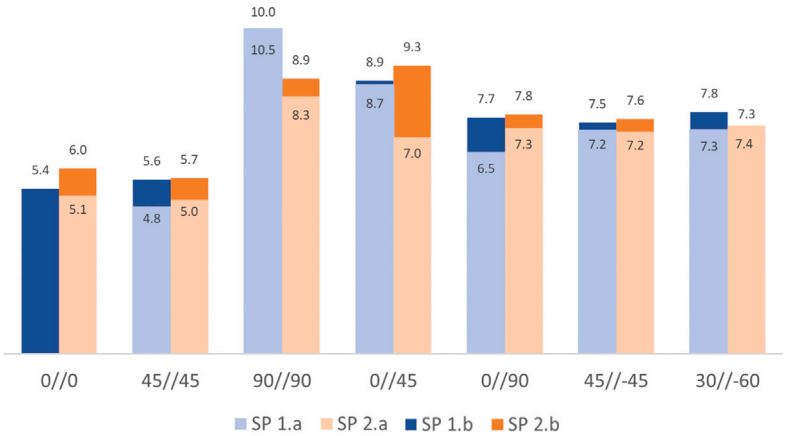

Fig. 10. The calibrated values for G_A (GPa).

Table 6
Material properties difference in absolute percent value for all seven interfaces. In the first two rows related to each property, a comparison between two specimens of the same interface in the same test stage is presented. In the two latter rows for each property, a comparison of the change between the first and second stage of a fatigue test for the same specimen is shown. Data regarding 0°//0° SP 1.a is not available due to an error in data acquisition.

Specimen	0°//0°	45°//45°	90°//90°	0°//45°	0°//90°	45°//−45°	30°//−60°
E_A							
SP 1.a vs. SP 2.a	N.A	4.7	26.1	41.4	10.7	0.1	2.0
SP 1.b vs. SP 2.b	4.5	1.0	12.2	16.6	1.4	1.0	8.0
SP 1.a vs. SP 1.b	N.A	7.4	5.1	4.8	14.7	0.1	7.4
SP 2.a vs. SP 2.b	14.8	3.9	6.5	21.4	5.8	1.0	2.0
E_T							
SP 1.a vs. SP 2.a	N.A	5.3	26.1	23.1	8.5	1.0	1.0
SP 1.b vs. SP 2.b	10.3	0.0	12.2	2.8	12.3	3.8	10.0
SP 1.a vs. SP 1.b	N.A	9.2	5.1	0.0	16.8	4.5	9.1
SP 2.a vs. SP 2.b	14.2	4.1	6.5	21.1	20.2	9.1	1.0
G_A							
SP 1.a vs. SP 2.a	N.A	4.7	26.1	24.1	10.8	0.4	1.9
SP 1.b vs. SP 2.b	10.8	1.0	12.2	5.2	1.4	1.4	8.0
SP 1.a vs. SP 1.b	N.A	15.5	5.1	1.5	14.7	3.4	7.4
SP 2.a vs. SP 2.b	14.6	12.3	6.5	24.8	5.7	5.2	1.9

first comparison evaluated the differences between two specimens of the same interface at the same test stage. The specimens are referred as 1 or 2 for the first and second specimens, respectively. The second comparison examined the change of the calibrated material properties between the first and second stage of a fatigue test for the same specimen, referred to as 'a' or 'b', respectively. Results for the former comparison are shown in Table 6 in the first two rows, related to each material property, namely, SP 1.a vs. SP 2.a and SP 1.b vs. SP 2.b. The results are displayed as absolute percentage values. The results for the latter comparison are shown in the third and fourth rows of Table 6, namely, SP *i.a* vs. SP *i.b* with $i = 1$ in the third row and $i = 2$ in the fourth.

From Figs. 8 through 10, and the values in Table 6, it can be observed that the 45°//45°, 0°//0°, 30°//−60°, and 45°//−45° interfaces, where specimens with the same layup in the same test stage are compared, exhibit relatively similar mechanical properties, with a maximum difference of 10.8% between SP 0°//0°.1.b and SP 0°//0°.2.b. In contrast, for the 90°//90°, 0°//45°, and 0°//90° interfaces, more significant differences were observed: up to 41.4% between SP 0°//45°.1.a and SP 0°//45°.2.a, and 26.1% between SP 90°//90°.1.a and SP 90°//90°.2.a for the short delamination test stage specimens. These differences decreased to a maximum of 16.6% and 12.2% for SP 0°//45°.1.b vs. SP 0°//45°.2.b and for SP 90°//90°.1.b vs. SP 0°//45°.2.b, respectively, in the long delamination test stage.

These results suggest that certain interfaces show minimal scatter in mechanical properties between specimens with the same layup and similar short or long initial delamination lengths, consistent with the progressive nature of LSB as the delamination length increases. However, for interfaces such as 90°//90°, 0°//45°, and 0°//90°, higher variation and less consistent results were observed for specimens tested in the short delamination test stage, when LSB was not fully developed. Once the steady state was reached, the scatter between these specimens decreased. It is noteworthy that these interfaces are more susceptible to extensive LSB [27,28], which may explain the observed variability. Furthermore, the reduction in discrepancies between the calibrated properties of specimens with long delaminations compared to those with short ones may indicate a convergence trend, potentially attributed to fiber bridging saturation.

Overall, this investigation suggests that specimens with interfaces more prone to increased LSB, such as 90°//90°, 0°//90°, and 0°//45°, tend to exhibit less consistent and more scattered calibrated material properties between specimens, with more pronounced stiffening between short and long delamination lengths. This observation implies that the scatter associated with delamination propagation in MD laminates may be related to the presence of LSB.

When investigating the results of the change in material properties between short and long delamination, specifically the latter two rows for every material property shown in Table 6, namely, rows (SP *i.a* vs. SP *i.b* with $i = 1, 2$), one may observe that, as expected, material stiffness increased with delamination length. This finding aligns with the hypothesis that the observed increase in fatigue resistance during delamination propagation testing of MD composites is directly linked to an increase in LSB [41,58]. Notably, the maximum increases in E_A, E_T, and G_A between the first and second test stages were observed in SP 0°//45°.2, with values of 21.4%, 21.1%, and 24.8%, respectively. In contrast, SP 0°//45°.1 exhibited much smaller increases, ranging from 0% to 4.8%. This discrepancy may indicate significant scatter associated with the development of LSB. Although the difference between the two specimens during the short delamination stage was 41.4%, this difference decreased to 16.4% during the long delamination stage, suggesting that LSB saturation has been reached.

In contrast to this general trend of increasing material properties with delamination length, for SP 90°//90° 1.b (depicted in dark blue) compared to SP 90°//90° 1.a (depicted in light blue), a decrease in E_A, G_A, and E_T was observed for the long delamination test stage compared to the short one. Hence, the dark blue column appears hidden. This finding diverges from the trend observed for all other specimens and interfaces related to increase of specimen toughening with delamination growth due to increasing LSB [58].

A plausible explanation for this behavior may be related to the complex delamination propagation observed for this interface, as seen in the images obtained during the test. These images revealed delamination oscillations and splitting. For example, in Fig. 11,

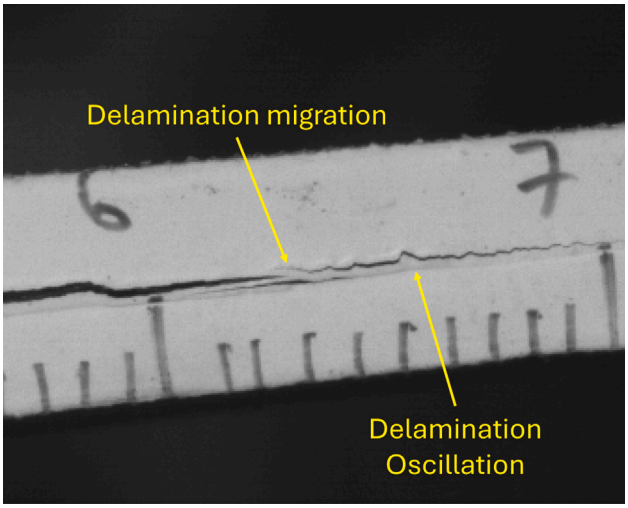

Fig. 11. Example of the delamination front image of SP 90°//90° 1.a. The image illustrates delamination front migration as well as the oscillatory behavior of the delamination front.

an image captured at cycle $N = 9000$ in the first test stage for SP 90°//90°.2 is presented, where the oscillations and splitting are evident. It is important to note that such behavior was not observed for the other interfaces. It may be assumed that the specimens with a 90°//90° interface were influenced by these multiple failure mechanisms, including LSB, occurring simultaneously. The pronounced oscillations and splitting at the delamination tip for this specimen could potentially complicate the application of linear elastic fracture mechanics (LEFM), which was used in the applied numerical modeling. Since LEFM typically assumes self-similar crack propagation with a single, well-defined crack tip, these complex behaviors may not align perfectly with its assumptions. To more accurately capture the delamination propagation in such cases, it might be beneficial to explore more advanced modeling strategies.

Another observation based on the compliance calibrated material properties obtained and shown in Figs. 8 through 10 and in Table 5, is that on average, the 90°//90°, 0°//45°, and 0°//90° interfaces exhibited the highest stiffness, with average E_A values for SP 1.b and SP 2.b of 275 GPa, 236.5 GPa, and 250 GPa, respectively. These average values represent a 77%, 52.5%, and 61% increase compared to the literature E_A value of 155 GPa, as shown in Table 2. In contrast, the 0°//0°, 45°//45°, and 30°//−60° interfaces, with average E_A values of 194 GPa, 197 GPa, and 212 GPa, respectively, showed an increase of 25%, 27%, and 36.7% over the literature E_A value.

These findings indicate that the 90°//90°, 0°//90°, and 0°//45° interfaces are most prone to LSB and, therefore, become the stiffest, while the 0°//0° interface is least influenced by LSB and, as a result, is the least stiff. This finding aligns with literature that demonstrates increased traction forces for the 0°//90° and 0°//45° interfaces compared to the 0°//0° interface [27]. Additionally, in Ref. [28], it was reported that MD interfaces exhibit higher fracture toughness than UD interfaces, with the 90°//90° interface being the toughest, followed closely by the 0°//45°, 0°//90°, and −45°//+45° interfaces, which displayed relatively similar traction values.

7.2. Paris plots comparison — Calibrated J-integral versus MCC

In this section, the resulting Paris plots of da/dN versus $\mathcal{G}_{Imax}$ are presented. The values of $\mathcal{G}_{Imax}$ were obtained using the global MCC method described in Section 3.2.1 and the local J-integral from Section 3.2.2 with FEAs employing the calibrated material properties from Table 5, as well as with the properties from the literature in Table 2. The obtained results are examined and compared. Additionally, a power fit of the form in Eq. (1) was applied to the results. The fitting parameters C and n, and the R^2 values for each fit are detailed in Table A.1.

In Fig. 12, Paris plots are presented for the specimens with an initial delamination between two similar plies, namely, 0°//0°, 45°//45°, and 90°//90°. Paris plots related to specimens with an initial delamination along an interface between two dissimilar materials, namely, 0°//45°, 0°//90°, 45°//−45°, and 30°//−60° are shown in Fig. 13. Recall that the results for SP 0°//0° 1.a are not shown in the figures due to faulty data acquisition. In the figures, results obtained using the MCC method are shown in blue and the values obtained using the J-integral and related to the material properties from the literature, namely the properties in Table 2 are in orange. The ERR values obtained from the J-integral with the calibrated material properties in Table 5 are presented in green. Recall that for each layup, two specimens were tested. In Figs. 12 and 13, the first tested specimen, for each interface, is marked with a triangle, and the second with a circle. Markers for tests with a short initial delamination length are filled, whereas those for representing a long initial delamination lengths are unfilled. For each test, the initial delamination length, which significantly influences the results, is specified in the plot.

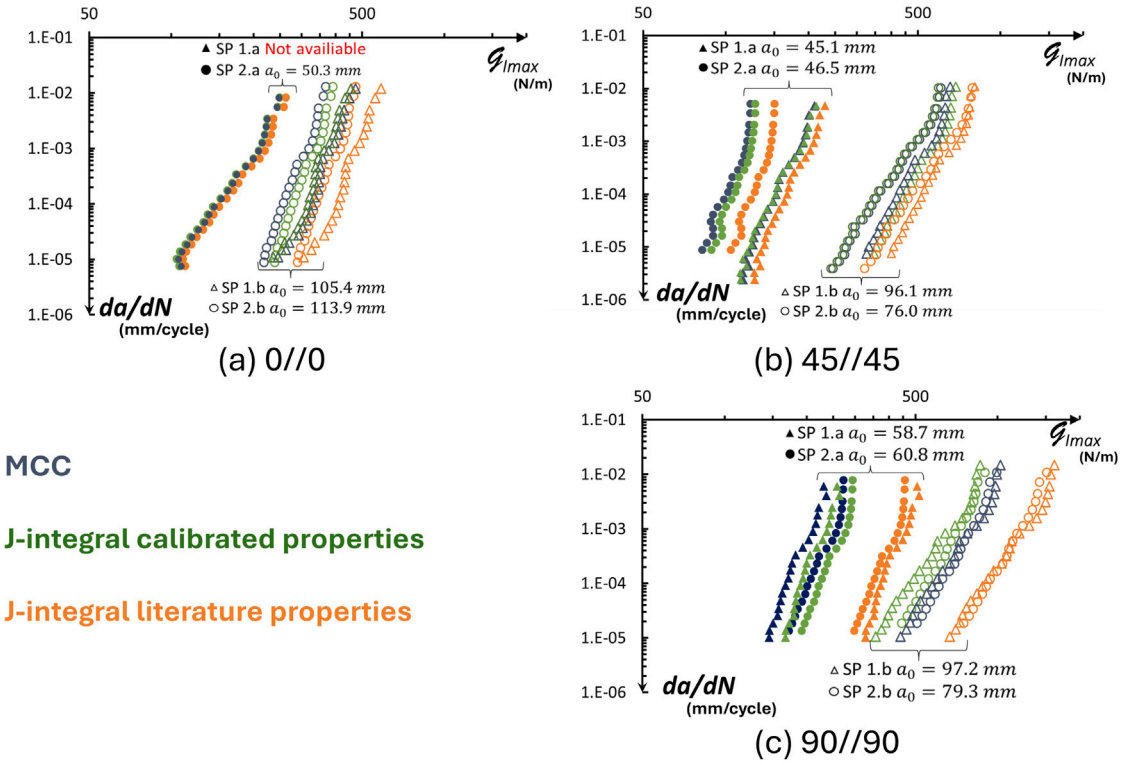

Fig. 12. The delamination propagation rate da/dN plotted against the maximal mode I ERR $\mathcal{G}_{I_{max}}$ in a fatigue cycle on a log–log scale. This is shown for all UD interfaces: (a) 0//0, (b) 45//45, and (c) 90//90. The results using MCC are depicted in blue; the J-integral with calibrated properties is in green, and the J-integral with properties from the literature is in orange. Data for the first and second specimens are represented by triangles and circles, respectively. Additionally, a_0 denotes the delamination length at the start of the fatigue test.

Upon examining the results in Figs. 12 and 13, it is evident that all specimens exhibit a noticeable rightward shift in their respective Paris plots as the delamination extended. A rightward shift in the Paris plots corresponds to an increase in fatigue resistance, as indicated by the increase in $\mathcal{G}_{I_{max}}$ values [23–25]. This shifting phenomenon is widely documented in the literature and is commonly attributed to the development of fiber bridging mostly during the quasi-static propagation of delamination across each testing stage [30,41,43].

Furthermore, Figs. 12 and 13 demonstrate that Paris plots derived from the J-integral using literature-based material properties are shifted to the right compared to those based on calibrated material properties. Moreover, the calibrated material properties are consistently higher than those from the literature, as shown in Table 5. This means that the FE model with literature-based properties exhibits greater displacement and compliance than the one with calibrated properties. Consequently, for the same applied load, the higher compliance of the literature-based model results in greater strains, stresses, and a higher calculated ERR compared to the less compliant calibrated model.

By extending this conclusion, one would anticipate that specimens exhibiting substantial differences between calibrated and literature properties would display a more pronounced rightward shift in the Paris plots. Indeed, this expectation holds. To quantify the rightward shift, the average relative difference in $\mathcal{G}_{I_{max}}$ between the calibrated and literature J-integral properties was calculated as

$$\Delta\mathcal{G}_{I_{max}} = \frac{1}{N_f}\sum_{i=0}^{N_f}\frac{\mathcal{G}_{cal(i)} - \mathcal{G}_{lit(i)}}{\mathcal{G}_{cal(i)}} \cdot 100(\%)\ , \tag{21}$$

where $\Delta\mathcal{G}_{I_{max}}$ represents the average percentage relative difference throughout the whole fatigue test, N_f is the total number of cycles in a fatigue test, and $\mathcal{G}_{cal(i)}$ and $\mathcal{G}_{lit(i)}$ are the maximum mode I ERR in cycle i calculated using the J-integral with calibrated and literature properties, respectively.

The resulting relative ERR average differences $\Delta\mathcal{G}_{I_{max}}$ between the literature and calibrated properties are plotted in Fig. 14 as a function of the relative increase in E_A (denoted as ΔE_A) with respect to the literature properties. A linear fit with an R^2 of 0.77, is presented in the figure indicating a strong linear correlation between the increase in fatigue resistance and the increase in specimen stiffness. The former is evident from the shift in Paris plots, and the latter from the calibrated properties related to the compliance of the specimen.

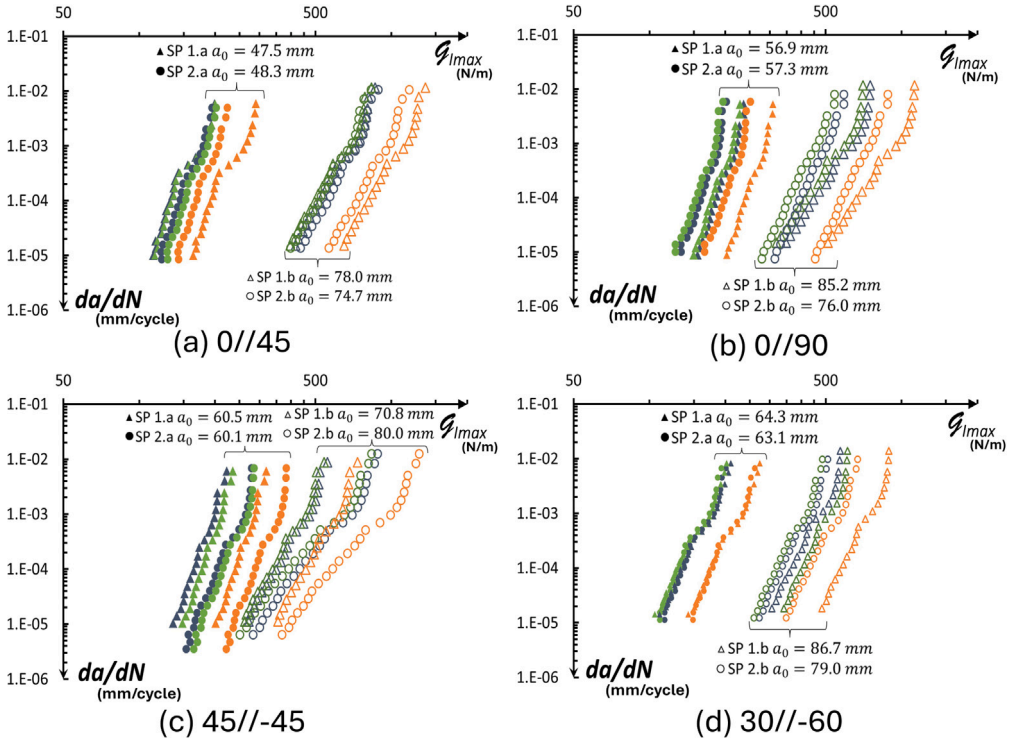

Fig. 13. The delamination propagation rate da/dN plotted against the maximal mode I ERR $\mathcal{G}_{I_{max}}$ in a fatigue cycle on a log–log scale. This is shown for all MD interfaces: (a) 0//45, (b) 0//90, (c) 45//−45, and (d) 30//−60. The results using MCC are depicted in blue, the J-integral with calibrated properties is in green, and the J-integral with properties from the literature is in orange. Data for the first and second specimens are represented by triangles and circles, respectively. Additionally, a_0 denotes the delamination length at the start of the fatigue test.

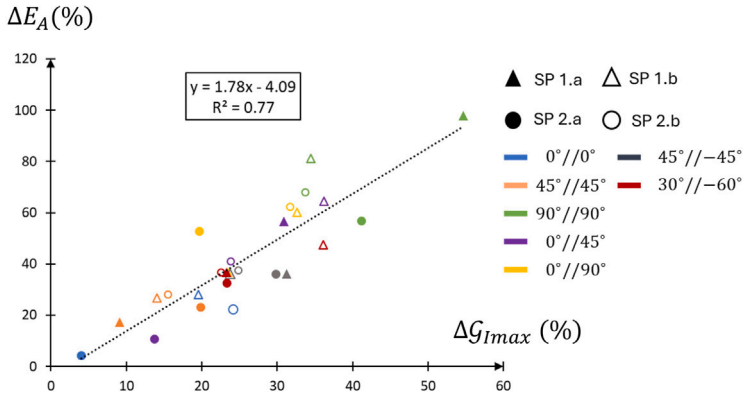

Fig. 14. The relative percent increase in E_A, denoted as ΔE_A, between the J-integral values calculated using the calibrated and literature material properties, is compared with the relative average ERR difference, $\Delta\mathcal{G}_{I_{max}}$, which is calculated according to Eq. (21) for the calibrated and literature material properties. The dashed line represents a linear trend line.

From Fig. 12.a, it is apparent that SP 0°//0° 2.a exhibits a small shift between the Paris curve related to calibrated (green) and literature (orange) properties. An average difference of 4.1% between calibrated and literature properties was quantified using Eq. (21). A similar pattern is observed for SP 0°//45° SP 2.a in Fig. 13.a, where the green and orange circles are rather close to each other, with an average difference of 13.7% calculated using Eq. (21). For these configurations, E_A increased from the literature value of 155 GPa to 161.6 GPa and 171.6 GPa for 0°//0° 2.a and 0°//45° SP 2.a, respectively, representing increases of 4.25% and 10.7%, respectively. Conversely, for SP 90°//90° 1.a and 2.a in Fig. 12.c, the average differences are significantly higher, at 54.7% and 41.2%, respectively, corresponding to increases in E_A of 136.1% and 87.6%.

In Fig. 15, Paris plots of da/dN versus $\mathcal{G}_{Imax}$ are shown for all layups. This plot enables examination of the relation between the fatigue resistance and the specimen interface layup. Note that since the calibrated J-integral results are consistent with the MCC

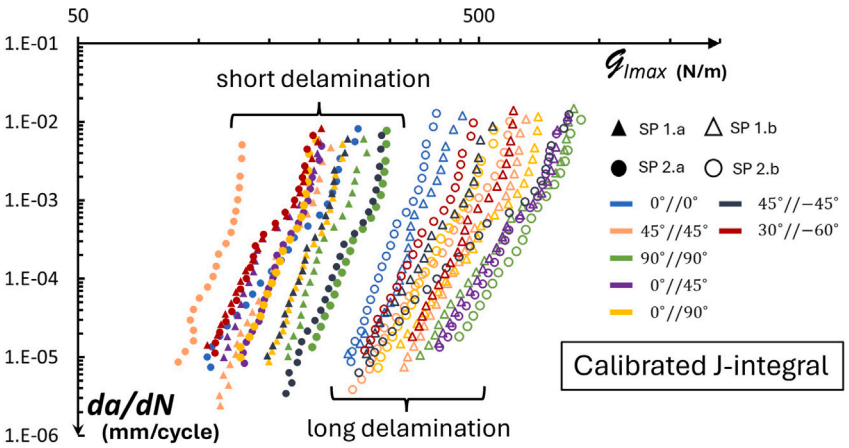

Fig. 15. The delamination propagation rate da/dN plotted against the maximal mode I ERR $\mathcal{G}_{I_{max}}$ in a fatigue cycle on a log–log scale. This is shown for all layups using the J-integral with the calibrated properties. data for the first and second specimens are represented by triangles and circles, respectively. Also, solid symbols represent the first testing stage with a short delamination while unfilled symbols represent the second testing stage with a long delamination.

analysis, only the $\mathcal{G}_{I_{max}}$ values obtained with the calibrated J-integral based on the FEA simulations with calibrated properties for all specimens and interfaces are shown.

From the data related to the second stage of testing (SP 1,2.b) in Fig. 15, it is evident that the 0°//0° layup marked in blue unfilled triangles for SP 1.b and blue unfilled circles for SP 2.b, exhibited the least resistance to fatigue delamination. Whereas the 90°//90° layup marked in green unfilled triangles for SP 1.b and green unfilled circles for SP 2.b demonstrates the highest resistance. This conclusion is drawn from the relative positions of the Paris plots, where the SP 0°//0° i.b ($i = 1, 2$) plots are positioned furthest to the left, and the SP 90°//90° i.b ($i = 1, 2$) plots are located furthest to the right. For the short delamination Paris plots, although the plot for SP 90°//90° 2.a is positioned furthest to the right, this trend does not hold for SP 90°//90° 1.a. Additionally, unlike the long delamination plots, SP 0°//0° 2.a is not positioned furthest to the left.

Overall, it appears that in the long delamination plots, there is greater separation between different interface layups, along with better grouping of specimens with the same layup configuration. From the long delamination plots, a fatigue resistance sequence among the different interfaces may be observed, ranging from least to most resistant as follows: 0°//0°, 30°// − 60°, 45°// − 45°, 45°//45°, 0°//90°, 0°//45°, and 90°//90°. This observation aligns with the calibrated stiffness values presented in Figs. 8 through 10, as SP 0°//0° i.b ($i = 1, 2$) shows the lowest average E_A of 193 GPa, while SP 90°//90° i.b ($i = 1, 2$) displays the highest average E_A of 275 GPa. Conversely, in the first stage of testing (SP 1,2.a), no discernible trends in fatigue delamination resistance are observed.

Another observation to be pointed is that the second stage data plots of both specimens of the same layup are closer to each other in comparison to the first stage data plots. This may imply that the specimens with the propagated delamination are reaching fiber bridging saturation to some degree which results in less scatter in the measured ERRs for different specimens. This is especially visible in SP 90°//90° 1,2.b and SP 45°// − 45° 1,2.b marked in green and dark gray, respectively.

8. Conclusions

When evaluating the fatigue delamination propagation behavior of composite laminates subjected to cyclic fatigue loading, it is crucial to consider the additional toughness provided by LSB, which results in crack tip shielding due to the bridging fibers. In this study, it was shown that for MD specimens and MD interfaces, the effect of LSB on general compliance, as well as the ERR required for propagation, differs and is increased compared to that of UD specimens. Therefore, a method is proposed to account for this additional toughness by augmenting the material stiffness of the specimens. The results in Figs. 12 and 13 demonstrate that this method yields good agreement between the MCC global computations for all seven layups tested, as well as for the two initial delamination lengths used in each specimen. This further validates the approach of incorporating the added tractions from LSB as a boost in material stiffness.

Additionally, upon examining Figs. 8 and 10, it may be seen how the specimens stiffness increases as the delamination propagates. This trend includes all analyzed specimens with the exception of SP 90°//90° 1, where unusual behavior contrary to the general trend was observed. Moreover, it is also evident that the 0°//0° interface specimens exhibited the least significant increase in stiffness compared to the literature material properties, while on average, the 90°//90°, 0°//45°, and the 0°//90° interface specimens showed the largest increase in stiffness relative to the literature material properties. These observations are supported by findings from the literature [27,28].

The lack of standardized fatigue test protocols and analysis methods for MD laminated composite laminates highlights the need for validated approaches to characterize their complex behavior. The variability in stiffness across different interfaces, as demonstrated in this study, underscores the importance of incorporating LSB into simulations, which can be achieved by accounting

for stiffening effects in the mechanical properties. Additionally, a potential relationship between fiber orientation along the interface and the amplitude of LSB stiffening was observed, although an attempt to quantify this stiffening requires further data for conclusive findings. Overall, the proposed method provides a validated numerical framework for both UD and MD DCB specimens when compared to the global MCC method. Future research could involve using this method in conjunction with a multi-stage fatigue test that incorporates more than two initial delamination lengths. The toughening observed during the material properties calibration process could then be used to establish a fatigue resistance curve, offering a tangible representation of the additional toughness attributed to LSB and contributing to a deeper understanding of this phenomenon.

CRediT authorship contribution statement

Roy Amkies: Writing – review & editing, Writing – original draft, Visualization, Validation, Software, Methodology, Investigation, Formal analysis, Conceptualization. **John-Alan Pascoe:** Writing – review & editing, Resources, Investigation, Data curation. **Mike van der Panne:** Resources, Investigation, Data curation. **Mor Mega:** Writing – review & editing, Supervision, Investigation, Conceptualization.

Declaration of competing interest

The authors declare that they have no known competing financial interests or personal relationships that could have appeared to influence the work reported in this paper.

Acknowledgment

Roy Amkies was partly supported by "DROR" scholarship provided by Ariel University.

Appendix. Paris plots coefficients

In this section, the coefficients of the Paris plots obtained in Section 7.2 are presented in Table A.1, with the corresponding R^2 values.

Table A.1
Paris relation C and n coefficients from the power fit with corresponding R^2 values. Presented for all tested specimens analyzed via MCC, calibrated material properties J-integral and literature material properties J-integral.

	C	n	R^2	C	n	R^2	C	n	R^2	C	n	R^2
0°//0°	SP 1.a			SP 1.b			SP 2.a			SP 2.b		
Calibrated J				3.30E−31	10.66	0.86	1.01E−19	6.93	0.91	1.30E−37	13.42	0.89
Literature J	Not available			1.87E−32	10.68	0.86	7.54E−20	6.91	0.91	7.96E−39	13.45	0.89
MCC				1.62E−31	10.71	0.87	4.28E−20	7.09	0.91	2.17E−35	12.70	0.90
45°//45°	SP 1.a			SP 1.b			SP 2.a			SP 2.b		
Calibrated J	6.06E−30	9.50	0.80	1.08E−29	11.41	0.88	6.19E−28	9.05	0.96	2.11E−31	12.23	0.82
Literature J	3.37E−26	10.34	0.80	3.50E−25	8.00	0.88	8.83E−30	11.50	0.96	3.43E−29	9.30	0.82
MCC	4.17E−27	10.36	0.80	3.19E−26	8.02	0.88	3.47E−32	12.36	0.96	4.72E−30	9.31	0.82
90°//90°	SP 1.a			SP 1.b			SP 2.a			SP 2.b		
Calibrated J	4.80E−30	8.54	0.91	4.07E−40	13.71	0.82	5.11E−27	8.38	0.83	1.16E−35	12.15	0.94
Literature J	1.86E−29	8.86	0.91	2.31E−33	12.83	0.82	2.66E−26	8.49	0.83	1.05E−30	11.23	0.94
MCC	4.63E−36	13.69	0.90	3.72E−24	7.24	0.82	2.75E−33	12.13	0.82	4.69E−28	8.52	0.93
0°//45°	SP 1.a			SP 1.b			SP 2.a			SP 2.b		
Calibrated J	3.71E−28	10.94	0.91	5.31E−26	7.89	0.84	8.67E−34	13.30	0.96	1.87E−27	8.40	0.90
Literature J	8.11E−29	10.48	0.90	1.07E−27	7.89	0.84	3.59E−34	13.21	0.95	1.06E−28	8.38	0.90
MCC	1.26E−27	10.72	0.90	1.12E−26	8.08	0.84	2.06E−32	12.80	0.96	1.81E−28	8.66	0.90
0°//90°	SP 1.a			SP 1.b			SP 2.a			SP 2.b		
Calibrated J	4.98E−35	13.44	0.87	1.88E−23	7.14	0.86	6.68E−32	12.44	0.79	6.05E−30	9.86	0.96
Literature J	7.47E−37	13.47	0.87	6.27E−25	7.14	0.86	2.03E−34	12.92	0.78	4.89E−32	9.86	0.96
MCC	1.79E−35	13.55	0.87	3.00E−24	7.34	0.86	1.89E−33	13.03	0.78	1.09E−31	10.35	0.96
45°// − 45°	SP 1.a			SP 1.b			SP 2.a			SP 2.b		
Calibrated J	1.41E−20	5.99	0.94	6.69E−33	12.71	0.88	2.84E−25	8.01	0.87	1.06E−29	10.79	0.84
Literature J	7.76E−35	13.39	0.94	6.80E−26	8.38	0.88	5.26E−32	11.68	0.87	1.65E−19	5.67	0.84
MCC	1.22E−36	13.40	0.95	5.11E−27	8.38	0.88	1.44E−33	11.71	0.87	6.58E−20	5.46	0.83
30°// − 60°	SP 1.a			SP 1.b			SP 2.a			SP 2.b		
Calibrated J	5.25E−29	9.20	0.92	4.26E−25	9.06	0.88	4.89E−32	9.86	0.91	3.48E−28	10.41	0.88
Literature J	5.16E−29	9.61	0.92	3.09E−24	9.14	0.88	1.09E−31	10.35	0.91	3.68E−27	10.49	0.88
MCC	6.98E−24	9.05	0.92	4.76E−30	9.71	0.88	8.80E−27	10.40	0.91	8.79E−29	9.60	0.89

Data availability

Data will be made available on request.

References

[1] ASTM D5528-13. Standard test method for mode I interlaminar fracture toughness of unidirectional fiber-reinforced polymer matrix composites. In: Space simulation; aerospace and aircraft; composite materials. vol. 15.03, West Conshohocken, PA: American Society for Testing and Materials; 2013.
[2] Wisnom M. The role of delamination in failure of fibre-reinforced composites. Philos Trans R Soc A: Math Phys Eng Sci 2012;370:1850–70.
[3] Bathias C. The fatigue of high performance composite materials. In: Advances in fatigue science and technology. Dordrecht: Springer Netherlands; 1989, p. 659–76.
[4] Yao L, Alderliesten R, Zhao M, Benedictus R. Bridging effect on mode I fatigue delamination behavior in composite laminates. Ompos. - A: Appl Sci 2014;63:103–9.
[5] Rhee KY, Koh SK, Lee JH. Mode I fracture resistance characteristics of graphite/epoxy laminated composites. Polym Compos 2000;21(2):155–64.
[6] Mega M, Dolev O, Banks-Sills L. Fracture toughness resistance curves for a delamination in CFRP MD laminate composites. Part II: Mixed-mode deformation. Theor Appl Fract Mech 2024;133:104583.
[7] Mega M, Dolev O, Banks-Sills L. Fracture toughness resistance curves for a delamination in CFRP md laminate composites, part I: Nearly mode II deformation. Theor Appl Fract Mech 2022;119:103335.
[8] Rehan M, Rousseau J, Fontaine S, Gong X. Experimental study of the influence of ply orientation on DCB mode-i delamination behavior by using multidirectional fully isotropic carbon/epoxy laminates. Compos Struct 2017;161:1–7.
[9] Raimondo A, Urcelay O, Bisagni C. Influence of interface ply orientation on delamination growth in composite laminates. J Compos 2021;55:3955–72.
[10] Lachaud F, Piquet R, Michel L. Delamination in mode I and II of carbon fibre composite materials: Fibre orientation influence. In: Proc. 12th international conference on composite materials, Paris, July. 1999.
[11] Allix O, Leveque D, Perret L. Identification and forecast of delamination in composite laminates by an interlaminar interface model. Compos Sci Technol 1998;58(5):671–8.
[12] Simon I, Banks-Sills L, Fourman V. Mode I delamination propagation and R-ratio effects in woven composite DCB specimens for a multi-directional layup. Int J Fatigue 2017;96:237–51.
[13] Chocron T, Banks-Sills L. Nearly mode I fracture toughness and fatigue delamination propagation in a multidirectional laminate fabricated by a wet-layup. Phys Mesomech 2019;22:107–40.
[14] Blondeau C, Pappas G, Botsis J. Influence of ply-angle on fracture in antisymmetric interfaces of CFRP laminates. Compos Struct 2019;216:464–76.
[15] Pichler N, Herráez M, Botsis J. Mixed-mode fracture response of anti-symmetric laminates: Experiments and modelling. Compos B Eng 2020;197:108089.
[16] De Morais A, De Moura M, Gonçalves J, Camanho P. Analysis of crack propagation in double cantilever beam tests of multidirectional laminates. Mech Mater 2003;35:641–52.
[17] Mega M, Banks-Sills L. Testing of Brazilian disk specimens with a delamination between a transversely isotropic and a tetragonal composite ply. Procedia Struct Integr 2018;13:123–30, ECF22 - Loading and Environmental effects on Structural Integrity.
[18] Farkash E, Banks-Sills L. Virtual crack closure technique for an interface crack between two transversely isotropic materials. Int J Fract 2017;205(2):189–202.
[19] Rice J. A path independent integral and the approximate analysis of strain concentration by notches and cracks. J Appl Mech 1968;35:379–86.
[20] Rybicki E, Kanninen M. A finite element calculation of stress intensity factors by a modified crack closure integral. Eng Fract Mech 1977;9:931–8.
[21] Singh A, Aizen S, Mega M, Rifkind S, Banks-Sills L. Fatigue delamination propagation: Various effects on results. Fatigue Fract Eng Mater Struct 2024;47(2):275–97.
[22] Mega M, Banks-Sills L. Mixed mode interface fracture toughness of a multi-directional composite–UD/woven pair. Theor Appl Fract Mech 2019;104:102323.
[23] Sørensen BF, Jacobsen TK. Large-scale bridging in composites: R-curves and bridging laws. Compos - A: Appl 1998;29(11):1443–51.
[24] Spearing S, Evans AG. The role of fiber bridging in the delamination resistance of fiber-reinforced composites. Acta Met Mater 1992;40(9):2191–9.
[25] Cox B, Marshall D. The determination of crack bridging forces. Int J Fract 1991;49:159–76.
[26] Bao G, Suo Z. Remarks on crack-bridging concepts. Appl Mech Rev 1992;45(8):355–66.
[27] Shokrieh M, Salamat-Talab M, Heidari-Rarani M. Dependency of bridging traction of DCB composite specimen on interface fiber angle. Theor Appl Fract Mech 2017;90:22–32.
[28] Gong Y, Chen X, Li W, Zhao L, Tao J, Zhang J, Hu N. Delamination in carbon fiber epoxy DCB laminates with different stacking sequences: R-curve behavior and bridging traction-separation relation. Compos Struct 2021;262:113605.
[29] van der Panne M. Effect of different fibre orientations at the interface on fatigue delamination growth (Master's thesis), TU Delft Aerospace Engineering; 2022.
[30] Yao L, Chuai M, Lyu Z, Chen X, Guo L, Alderliesten R. A proposal for similitude in characterizing fatigue delamination behavior with fibre bridging of carbon-fibre reinforced polymer composites. Eng Fract Mech 2024;295:109756.
[31] Paris P. A rational analytic theory of fatigue. Trends Eng 1961;13:9.
[32] Paris P, Erdogan F. A critical analysis of crack propagation laws. J Basic Eng 1963;85:528–33.
[33] Paris P. The fracture mechanics approach to fatigue. In: Agamore army mat. res. conf.. vol. 10, 1964, p. 107–32.
[34] Singh A, Aizen S, Mega M, Rifkind S, Banks-Sills L. Fatigue delamination propagation: Various effects on results. Fatigue Fract Eng Mater Struct 2023;42:1–23.
[35] Murri GB. Effect of data reduction and fiber-bridging on mode I delamination characterization of unidirectional composites. J Compos Mater 2014;48(19):2413–24.
[36] Zhang J, Peng L, Zhao L, Fei B. Fatigue delamination growth rates and thresholds of composite laminates under mixed mode loading. Int J Fatigue 2012;40:7–15.
[37] Peng L, Zhang J, Zhao L, Bao R, Yang H, Fei B. Mode I delamination growth of multidirectional composite laminates under fatigue loading. J Compos Mater 2011;45:1077–90.
[38] Yao L, Alderliesten R, Zhao M, Benedictus R. Discussion on the use of the strain energy release rate for fatigue delamination characterization. Compos - A: Appl Sci Manuf 2014;66:65–72.
[39] Alderliesten R, Brunner A. Determination of mode I fatigue delamination propagation in unidirectional fibre-reinforced polymer composites. Test Protoc 2019-2020.
[40] Alderliesten R. Fatigue delamination of composite materials – approach to exclude large scale fibre bridging. IOP Conf Ser Mater Sci 2018;388(1):012002.
[41] van der Panne M, Pascoe J. Fatigue delamination growth-is UD testing enough? Procedia Struct 2022;42:449–56.
[42] Jones R, Hu W, Kinloch AJ. A convenient way to represent fatigue crack growth in structural adhesives. FFEMS 2015;38(4):379–91.

[43] Yao L, Alderliesten R, Jones R, Kinloch A. Delamination fatigue growth in polymer-matrix fibre composites: A methodology for determining the design and lifing allowables. Compos Struct 2018;196:8–20.
[44] Zobeiry N, Reiner J, Vaziri R. Theory-guided machine learning for damage characterization of composites. Compos Struct 2020;246:112407.
[45] Reiner J, Vaziri R, Zobeiry N. Machine learning assisted characterization and simulation of compressive damage in composite laminates. Compos Struct 2021;273:114290.
[46] Sause MG, Schmitt S, Kalafat S. Failure load prediction for fiber-reinforced composites based on acoustic emission. Compos Sci Technol 2018;164:24–33.
[47] Califano A, Chandarana N, Grassia L, D'Amore A, Soutis C. Damage detection in composites by artificial neural networks trained by using in situ distributed strains. Appl Compos Mater 2020;27:657–71.
[48] Freed Y, Salviato M, Zobeiry N. Implementation of a probabilistic machine learning strategy for failure predictions of adhesively bonded joints using cohesive zone modeling. Int J Adhes Adhes 2022;118:103226.
[49] Freed Y, Zobeiry N, Salviato M. Development of aviation industry-oriented methodology for failure predictions of brittle bonded joints using probabilistic machine learning. Compos Struct 2022;297:115979.
[50] Jin H, An N, Jia Q, Ma X, Zhou J. A mesoscale computational approach to predict ABD matrix of thin woven composites. Compos Struct 2024;337:118031.
[51] Davidson B, Schapery R. Effect of finite width on deflection and energy release rate of an orthotropic double cantilever specimen. J Compos Mater 1988;22(7):640–56.
[52] Rodi R, Alderliesten R, Benedictus R. Crack-tip behavior in fiber/metal laminates by means of digital image correlation. J Aircr 2010;47:1636–46.
[53] ISO 15024:2001(E). Fiber reinforced plastic composites - determination of mode i interlaminar fracture toughness, G_{Ic}, for unidirectional reinforced materials. Switzerland: International Organization for Standardization; 2001.
[54] Systèmes D. Abaqus, finite element analysis software. 2021.
[55] Mixed mode interface fracture toughness of a multi-directional composite – UD/woven pair. Theor Appl Fract Mech 2019;104:102323.
[56] Pedregosa F, Varoquaux G, Gramfort A, Michel V, Thirion B, Grisel O, Blondel M, Prettenhofer P, Weiss R, Dubourg V, Vanderplas J, Passos A, Cournapeau D, Brucher M, Perrot M, Duchesnay E. Scikit-learn: Machine learning in python. JMLR 2011;12:2825–30.
[57] Rasmussen CE, Williams CK, et al. Gaussian processes for machine learning, vol. 1, Springer; 2006.
[58] Yao L, Alderliesten R, Benedictus R. The effect of fibre bridging on the Paris relation for mode I fatigue delamination growth in composites. Compos Struct 2016;140:125–35.